Analysis of laser absorption gas sensors employing scanned-wavelength modulation spectroscopy with 1*f*-phase detection

Wen Yu Peng[1] · **Christopher L. Strand**[1] · **Ronald K. Hanson**[1]

Abstract

The recently introduced wavelength-modulation spectroscopy with 1*f*-phase detection (WMS-θ_{1f}) technique showed promising results with potentially improved measurement precision over the popular 1*f*-normalized WMS-*nf* (WMS-*nf*/1*f*) technique. Like WMS-*nf*/1*f*, WMS-θ_{1f} enjoys the typical benefits of WMS methods, including low-frequency noise rejection, correction for non-absorbing losses, and insensitivity to the broadband absorption spectra of interfering species. In this work, we performed a detailed analysis of the spectrally resolved scanned-wavelength WMS-θ_{1f} measurement technique and its direct comparison against the expected performance of scanned-wavelength WMS-*nf*/1*f* and scanned-wavelength direct-absorption spectroscopy (SDAS) measurements. This simulation-based analysis identified specific operating regimes in which the performance of WMS-θ_{1f} measurements in terms of accuracy is expected to be greater than the performance of WMS-*nf*/1*f* or SDAS. Additionally, improved guidelines for the optimal selection of laser-tuning parameters, including an explicit optimization of the optical scan depth parameter, were developed. Experiments with a CO_2 static cell perturbed by a high-speed air jet corroborated the simulation-based findings. Finally, a practical demonstration of a WMS-θ_{1f} sensor for measuring temperature and H_2O mole fraction in the exhaust of a CH_4/air flat-flame burner was presented, with the results confirming model predictions of the superior precision of WMS-θ_{1f} relative to WMS-*nf*/1*f* and SDAS.

1 Introduction

Tunable diode-laser absorption spectroscopy (TDLAS) is a proven technology widely utilized in combustion, hypersonics, industrial process control, and environmental sensing for quantitative in situ measurements of multiple gas properties such as species concentration, temperature, pressure, and velocity [1–5]. Scanned-wavelength direct-absorption spectroscopy (SDAS), in which gas parameters are inferred from the measured transmission fraction of a laser source as it tunes across absorption features of a target species, is the most widely used TDLAS technique due to its simplicity and robustness in relatively quiescent environments. For harsh environments where signal distortions such as optical emission, beam-steering, étalons, and general engineering

noise are substantial, wavelength modulation spectroscopy (WMS) is the preferred measurement technique due to its ability to suppress the effects of many forms of signal distortions. This is accomplished by modulating the wavelength of the laser at a high frequency, thereby encoding information related to the absorption spectrum at high frequencies and rejecting low-frequency distortions with lock-in filters. Further, wavelength-independent multiplicative signal distortions (e.g. beam-steering) can be corrected with the 1*f*-normalized WMS-*nf* detection scheme (for $n > 2$ and referred to as WMS-*nf*/1*f*), thereby enabling a calibration- and background-free gas absorption measurement technique. In exchange for added sensor design and signal-processing complexity, WMS-*nf*/1*f* is demonstratively a better measurement technique than SDAS for noisy conditions and has been successfully deployed in a variety of harsh environments that hinder SDAS sensing [6–13].

Until recently, researchers have focused on optimizing, analyzing, and deploying WMS-*nf*/1*f* sensors for diverse environments. A new WMS-based technique, here referred to as WMS-1*f*-phase detection (shortened to WMS-θ_{1f} or θ_{1f}), was only recently introduced and explored in several

✉ Wen Yu Peng
wypeng@stanford.edu

1 Department of Mechanical Engineering, Thermosciences Division, Stanford University, 452 Escondido Mall, Stanford, CA 94305, USA

publications [14, 15]. In WMS-θ_{1f}, the phase angle of the 1st harmonic is used for detecting gas absorption. The resulting WMS-θ_{1f} signal as the laser is tuned across an absorption feature approximately tracks the first derivative of the absorption spectrum and, therefore, is sensitive to both absorption linestrength and lineshape. Additionally, WMS-θ_{1f} signals enjoy all of the standard benefits of WMS-nf/1f such as beam-steering-distortion- and 1/f-additive-noise-rejection. The measured θ_{1f} signal can then be fitted with a lineshape model to infer gas properties using a fitting routine similar to the algorithm presented in Goldenstein et al. [16]. Also, since the technique utilizes only the 1st harmonic of the transmitted intensity waveform, it is easier to select appropriate modulation frequencies for frequency-domain multiplexing of multiple lasers [17] onto the same detector without encountering cross-talk issues between the nf harmonics of the modulation signal.

Yang et al. [14] presented a theoretical description and experimental demonstration of the WMS-θ_{1f} method for CO_2 detection in a static gas cell. Upadhyay et al. [15] presented a theoretical description and experimental demonstration of the WMS-R_{1f}/Y_{1f} method (which carries the same information as θ_{1f} and is, therefore, indistinct. See Sect. 2.2 for clarification) also for CO_2 detection in a static gas cell and the exhaust of a jet engine combustor. Both research teams directly compared the WMS-θ_{1f} or -R_{1f}/Y_{1f} results against WMS-$2f$/1f results and demonstrated that the new techniques performed better than WMS-$2f$/1f in terms of Allan variance and accuracy. However, these comparisons were performed using identical laser-tuning parameters for both the θ_{1f} and WMS-$2f$/1f measurements rather than at optimized laser-tuning parameters for each respective measurement technique. To appropriately demonstrate the superior performance of WMS-θ_{1f} relative to WMS-$2f$/1f, the laser-tuning parameters should be set at optimal conditions for each method independently.

In this work, we extended the framework developed in Yang et al. and Upadhyay et al. and performed an analysis of the WMS-θ_{1f} measurement technique and its expected performance in harsh environments. This analysis included a theoretical description of WMS-θ_{1f} (Sect. 2.2), a discussion on the WMS-θ_{1f} spectral fitting routine (Sect. 2.3), and a numerical assessment of the technique's sensitivity to environmental distortions commonly encountered in harsh measurement environments (Sects. 3.2 and 3.3). The new distortion analysis techniques also enabled the direct comparison of the expected performance of WMS-θ_{1f}, WMS-nf/1f, and SDAS in arbitrary measurement environments, leading to new guidelines for selecting the optimal measurement strategy and laser-tuning parameters. These guidelines are distinct from procedures previously reported in the literature

[8, 17, 18]. They represent the first-reported analysis and optimization scheme that (1) quantitatively identifies the measurement technique (out of WMS-θ_{1f}, nf/1f, and SDAS) that is expected to perform best for a given TDLAS application and (2) identifies laser operating parameters that explicitly minimize the impact of environmental signal distortions on the accuracy of WMS- or SDAS-based spectroscopic measurements. Several important results were achieved from this analysis.

1. Assuming broadband 1/f stochastic additive and multiplicative environmental signal distortions (e.g. optical emission and beam-steering), WMS-θ_{1f} measurements are generally more accurate than all WMS-nf/1f and SDAS techniques regardless of the selected laser-tuning parameters.
2. The optical scan depth parameter, often neglected in laser-tuning parameter optimization procedures for spectrally resolved WMS-nf/1f techniques, significantly affects the accuracy of all WMS-based measurement techniques. Simulations and experiments (Sects. 3.2.2 and 4.1) suggest selecting modulation and scan depths that obey certain linear relationships to minimize the expected error.
3. The frequency-domain characteristics of the stochastic signal distortions dictate the relative performance of the various WMS measurement techniques. Assuming the spectral amplitude of the distortions decays as a function of 1/f^p for some roll-off exponent, p, it was found that, above a certain value of p, WMS-nf/1f measurements became more accurate than WMS-θ_{1f} measurements. This provides useful guidelines for selecting the best WMS technique for a given measurement environment.
4. Conversely, for signal distortions with p near zero (i.e. white noise), the performance of SDAS-based sensors was found to exceed WMS-nf/1f-based sensors while rivaling the performance of WMS-θ_{1f}. This demonstrates that there are certain environments in which the use of WMS instead of SDAS is actually detrimental to the performance of a TDLAS sensor.
5. WMS-θ_{1f} is qualitatively as sensitive to wavelength-dependent distortions (e.g. étalons) as WMS-$2f$/1f. Similar to WMS-$2f$/1f, the measurement accuracy is less adversely impacted by étalon distortions with free spectral ranges that are sufficiently small or large relative to the absorption linewidth.
6. Short-period étalon distortions were found to impact the accuracy of SDAS measurements more strongly than WMS-θ_{1f}. For applications using long optical cavities (e.g. cavity-enhanced techniques) where étalon interfer-

ence fringes generally exhibit low free-spectral range, it may be beneficial to use WMS-θ_{1f} instead of SDAS.

The findings of the simulation-based analysis were corroborated with experimental measurements of CO_2 in a static cell with the laser beam perturbed by a high-speed air jet in free space to simulate broadband environmental distortions. Results from these experiments demonstrate the improved accuracy and precision of the WMS-θ_{1f} results against all WMS-nf/$1f$ and SDAS strategies in distortion environments with specific frequency characteristics. The WMS-θ_{1f} technique was then practically demonstrated by measuring the temperature and mole fraction of H_2O within the combustion product stream of a CH_4/air flat-flame burner. Allan deviations of the WMS-θ_{1f} results were found to be lower than the Allan deviations of the various WMS-nf/$1f$ techniques, further demonstrating the utility of the WMS-θ_{1f} technique for high-precision measurements in harsh environments.

2 Scanned-WMS-1f-phase detection principles

The scanned-WMS-1f-phase detection technique is grounded in WMS theory, which is well documented in the literature [17–21]. The fundamentals of LAS and WMS are briefly reviewed in this section to clarify notation. These are followed by a theoretical description of WMS-θ_{1f} signals and a discussion on the spectral fitting routine used to infer lineshape parameters from a θ_{1f} measurement. Additional nuances related to the θ_{1f} fitting routine not seen in typical WMS-nf/$1f$ fitting routines are highlighted and discussed.

2.1 Laser absorption spectroscopy

The spectral transmissivity, τ_ν, defined as the ratio between the transmitted (I_t) and incident (I_0) intensities, of monochromatic radiation with frequency ν (cm^{-1}) through a uniform ideal gas is described by the Beer–Lambert relation:

$$\tau_\nu = \left(\frac{I_t}{I_0}\right)_\nu = \exp(-\alpha_\nu) = \exp\left\{-\sum_k S_k P \chi L \phi_{\nu,k}\right\}, \quad (1)$$

where α_ν is the spectral absorbance, S_k (cm^{-2} atm^{-1}) is the linestrength of the kth absorbing transition, P (atm) is the absolute gas pressure, χ is the mole fraction of the absorbing species, L (cm) is the optical path length, and $\phi_{\nu,k}$ (cm) is the frequency-dependent normalized lineshape of the kth absorbing transition. S_k is purely a function of temperature, physical constants, and known molecular parameters [22] and can be calculated as follows:

$$S_k(T) = S_k(T_0)\frac{T_0}{T}\frac{Q(T_0)}{Q(T)}\exp\left[-\frac{hcE_j''}{k_B}\left(\frac{1}{T}-\frac{1}{T_0}\right)\right]$$
$$\times\left[1-\exp\left(-\frac{hc\nu_{0,k}}{k_B T}\right)\right]\left[1-\exp\left(-\frac{hc\nu_{0,k}}{k_B T_0}\right)\right]^{-1}, \quad (2)$$

where $S_k(T_0)$ is the linestrength at some reference temperature T_0 (296 K throughout this work), Q is the total internal partition function of the absorbing species, E_k'' (cm^{-1}) is the lower state energy of the transition, and $\nu_{0,k}$ (cm^{-1}) is the transition vacuum linecenter. The constants h (erg s), c (cm s^{-1}), and k_B (erg K^{-1}) are the Planck constant, speed of light, and Boltzmann constant, respectively.

The normalized Voigt lineshape function, which accounts for Doppler and collisional broadening effects, is widely used to model $\phi_{\nu,k}$. These effects are characterized by the Doppler broadening full-width half-maximum (FWHM), $\Delta\nu_D$ (cm^{-1}), and the collisional broadening FWHM, $\Delta\nu_C$ (cm^{-1}), given by

$$\Delta\nu_D = \nu_0\sqrt{\frac{8\ln(2)k_B T}{mc^2}} \quad (3)$$

$$\Delta\nu_C = 2P\sum_k \chi_k \gamma_{k,0}\left(\frac{T_0}{T}\right)^{n_k}, \quad (4)$$

where m (g) is the absorbing species molecular mass, $\gamma_{k,0}$ (cm^{-1} atm^{-1}) is the collisional broadening coefficient of the kth colliding species at the reference temperature, and n_k is the temperature-dependent exponent of the broadening coefficients.

For measurements of T, P, or χ in spectrally resolved TDLAS, it is often convenient to define the integrated absorbance, A_k (cm^{-1}), as the integral of the absorbance for a single absorption transition:

$$A_k = \int_{-\infty}^{\infty} S_k P \chi L \phi_k(\nu)d\nu = S_k P \chi L. \quad (5)$$

2.2 Scanned-WMS-θ_{1f}

Extensive information describing scanned-WMS can be found in the literature [16, 21, 23]; therefore, only a brief overview of its theoretical framework and its relation to WMS-θ_{1f} is provided here. WMS fundamentally involves modulating the laser injection current with a sinusoidal waveform of frequency f_m to tune the laser wavelength around the linecenter of an absorption feature. In scanned-WMS, an additional lower frequency sinusoidal scanning waveform of frequency f_s is added to the high-frequency modulation to produce spectrally resolved WMS signals

that can be used for lineshape fitting. The intensity ($I_0(t)$) and optical frequency ($\nu(t)$) response of a laser to sinusoidal injection-current tuning can be described as general Fourier series:

$$I_0(t) = \overline{I_0}\left[1 + \sum_{k=1}^{\infty} i_{s,k} \cos(2\pi k f_s t + \psi_{s,k}) \right.$$
$$\left. + \sum_{k=1}^{\infty} i_{m,k} \cos(2\pi k f_m t + \psi_{m,k})\right], \qquad (6)$$

$$\nu(t) = \overline{\nu} + \sum_{k=1}^{\infty} a_{s,k} \cos(2\pi k f_s t + \phi_{s,k})$$
$$+ \sum_{k=1}^{\infty} a_{m,k} \cos(2\pi k f_m t + \phi_{m,k}), \qquad (7)$$

where the subscripts s and m denote parameters associated with the low-frequency scan and high-frequency modulation, respectively. $\overline{I_0}$ is the mean intensity, i_k are the normalized intensity scan or modulation amplitudes, ψ_k are the intensity scan or modulation phases, $\overline{\nu}$ (cm^{-1}) is the mean optical frequency, a_k (cm^{-1}) are the optical scan or modulation depths, and ϕ_k are the wavelength scan or modulation phases. The index terms $k = 1$ and $k > 1$ represent the linear and nonlinear modulation components, respectively, with $i_1 \gg i_{k>1}$ and $a_1 \gg a_{k>1}$ in general. All laser response parameters can be characterized in the laboratory and do not change significantly over time for a given sensor system and laser settings.

It is useful to define the modulation and scan indices (μ and σ, respectively) as the linear optical modulation and scan depths ($a_{m,1}$ and $a_{s,1}$, respectively) non-dimensionalized by the lineshape half-width half-maximum of the targeted absorption transition. Different absorption spectra and laser-tuning parameters yield similar results when compared using these non-dimensional parameters. For a single absorption transition described by a Voigt profile, μ and σ can be approximated as follows:

$$\mu = 2a_{m,1}/(\Delta\nu_C + \Delta\nu_D), \qquad (8)$$

$$\sigma = 2a_{s,1}/(\Delta\nu_C + \Delta\nu_D). \qquad (9)$$

The interaction between $I_0(t)$, $\nu(t)$, and the spectral transmissivity (τ_ν) through the probed gaseous medium introduces new frequency content at the harmonics of f_m and beat frequencies of f_s and f_m in the transmitted intensity, $I_t(t)$. The resulting analytical expression for $I_t(t)$ is highly complex (see Appendix A in [21], for example) and most practical implementations of WMS simulate rather than analytically compute the harmonic signals [23]. To understand the qualitative behavior of scanned-WMS signals, it is more instructive to restrict the analysis to assume (1) no low-frequency scan (i.e. $i_{s,k} = a_{s,k} = 0$), (2) nonlinear terms are neglected (i.e. $i_{m,k>1} = a_{m,k>1} = 0$), and (3) $\phi_{m,1} = 0$, which is achieved in practice by setting an appropriate temporal offset in the data time series. With this simplification, $I_t(t)$ can be written as follows:

$$I_t(t) = G_{opt} I_0(t) \cdot \tau(\nu(t))$$
$$= G_{opt}\overline{I_0}\left[1 + i_{m,1}\cos(2\pi f_m t + \psi_{m,1})\right] \cdot \sum_{k=0}^{\infty} H_k \cos(2\pi k f_m t), \qquad (10)$$

where G_{opt} is some constant experimental opto-electronic detection gain and H_k are the cosine-series coefficients of the time-domain spectral transmissivity function:

$$H_k = \begin{cases} \frac{1}{2\pi}\int_{-\pi}^{\pi} \tau(\overline{\nu} + a_{m,1}\cos\theta)\mathrm{d}\theta & \text{if } k = 0, \\ \frac{1}{\pi}\int_{-\pi}^{\pi} \tau(\overline{\nu} + a_{m,1}\cos\theta)\cos k\theta\,\mathrm{d}\theta & \text{if } k \neq 0. \end{cases} \qquad (11)$$

We can now define the nth harmonic WMS signal, R_{nf}, to be the complex Fourier coefficient of the transmitted intensity corresponding to frequency nf_m, which is extracted from practical measurements using a lock-in/low-pass filter operation:

$$R_{nf} = \mathrm{LPF}(t) * \left[I_t(t) \cdot \exp(j2\pi n f_m t)\right], \qquad (12)$$

where LPF(t) is the impulse response function of the low-pass filter, $*$ is the convolution operator, and j is the imaginary unit. Combining Eqs. 10, 11, and 12, the expression for the complex phase angle of R_{1f}, θ_{1f}, can be given as follows:

$$\theta_{1f} = \angle(R_{1f}),$$
$$= \tan^{-1}\left\{\frac{i_{m,1}\sin\psi_{m,1}\left(H_0 - \frac{H_2}{2}\right)}{H_1 + i_{m,1}\cos\psi_{m,1}\left(H_0 + \frac{H_2}{2}\right)}\right\}. \qquad (13)$$

This expression can be viewed as the WMS-1f phase for a single center optical frequency, $\overline{\nu}$. By varying the center optical frequency with a low-frequency scan, a spectrally resolved θ_{1f} signal can be measured. An example of such a signal is shown in the bottom panel of Fig. 1 for single-Voigt profiles of various integrated absorbances and constant $\Delta\nu_C = 0.1$ cm^{-1} and $\Delta\nu_D = 0.01$ cm^{-1}. Note that the arctangent function used to calculate $\angle(R_{1f})$ throughout this work is the two-parameter arctangent function with output space $\in [-\pi, \pi]$. This choice was arbitrary and has no effect on results when compared to the standard single-parameter arctangent function with output space $\in [-\pi/2, \pi/2]$. Several important characteristics related to θ_{1f} can be observed from Eq. 13 and Fig. 1.
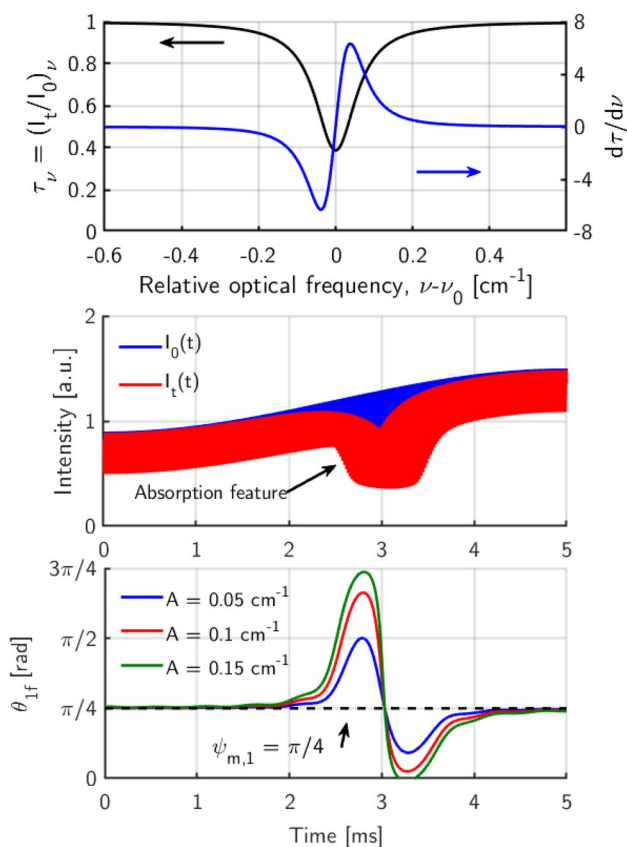
Fig. 1 (Top panel) Spectral transmissivity (black) and its derivative (blue) of an example absorption transition described by a single Voigt profile with $A = 0.15$ cm^{-1}, $\Delta\nu_C = 0.1$ cm^{-1}, and $\Delta\nu_D = 0.01$ cm^{-1}. (Middle panel) Simulated incident (blue) and transmitted laser intensity (red) for a scanned-WMS signal with $a_{m,1} = 0.1$ cm^{-1} and $a_{s,1} = 0.5$ cm^{-1}. (Bottom panel) The resulting WMS-θ_{1f} signals for various integrated absorbances. Note how the θ_{1f} amplitude scales with A and qualitatively tracks the profile of dτ/dν

1. Similar to WMS-nf/$1f$ signals, θ_{1f} signals are independent of $G_{opt}\overline{I_0}$ (as shown in Eq. 13) and, therefore, do not require *in situ* intensity calibration while naturally correcting for additive and multiplicative signal distortions such as optical emission, beam-steering, vibrations, and particulate matter occlusion with frequency-domain bandwidth below f_m/2.

2. In the absence of absorption, $\theta_{1f} = \psi_{m,1}$, which is simply the phase of the intensity modulation waveform. Additional temporal offsets in the data acquisition system will similarly manifest as constant phase offsets in the θ_{1f} signal that can be fitted as part of the spectral fitting routine. This is unlike the phase-sensitive WMS-R_{1f}/Y_{1f} (equivalent to $|R_{1f}|$/Im(R_{1f}) in the current nomenclature) detection strategy used in Upadhyay et al. [15].

3. H_1 is the dominant contributor to changes in θ_{1f} relative to the non-absorbing background. As noted in Reid and Labrie [18], $H_1 \propto -$dτ/dν in the $a_{m,1} \to 0$ limit. There-
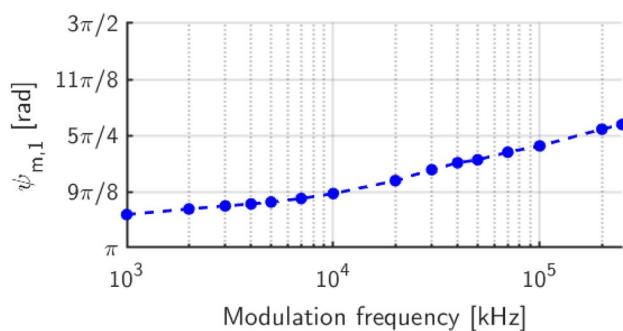

Fig. 2 Phase offset between the intensity- and optical frequency-modulation waveforms as a function of modulation frequency for an injection-current-tuned distributed-feedback tunable diode laser operating near 1.47 μm

fore, the scanned-θ_{1f} signal approximately tracks the first derivative of the transmission spectrum as shown in the top panel of Fig. 1. Additionally, since dτ/dν is a function of the absorption spectrum, θ_{1f} signals respond directly to the thermodynamic conditions of the absorbing species and, therefore, can be used for spectroscopic measurements.

4. θ_{1f} does not respond meaningfully to absorption if the phase offset between the intensity modulation waveform and the wavelength modulation waveform is close to a multiple of π (i.e. $\sin(\psi_{m,1}) \approx 0$). In practice, the thermal mass of typical semiconductor laser optical cavities acts as a low-pass filter with some ohmic heating-induced phase lag between the optical and intensity tuning waveforms, resulting in $\pi < \psi_{m,1} < 3\pi/2$ [24]. This lag is further pronounced and asymptotes towards $3\pi/2$ at high modulation frequencies as evidenced in Fig. 2 for a distributed-feedback tunable diode laser (DFB-TDL) operating near 1.47 µm (NEL Photonics). As will be shown in Sect. 3.2, θ_{1f} signals are least sensitive to environmental distortions when $\psi_{m,1} = 3\pi/2$.

2.3 Fitting of WMS-θ_{1f} signals

The fitting routine used to fit a simulated scanned-θ_{1f} signal, $\theta_{1f,sim}(t)$, to a measured θ_{1f} signal, $\theta_{1f,meas}(t)$, is similar to the least-squares WMS spectral fitting routine described in Goldenstein et al. [16] but with several important differences. A flowchart describing the algorithm is shown in Fig. 3. First, the user initializes guess values for the spectroscopic parameters associated with the Voigt lineshape profile (A, ν_0, $\Delta\nu_C$) and a background phase, δ [rad]. Note that $\Delta\nu_D$ can be calculated from temperature using Eq. 3, which in many cases is either well known or can be inferred by probing multiple absorption transitions of the same species. Hence, $\Delta\nu_D$ is generally a fixed value within the fitting routine. Next, these Voigt profile parameters are combined
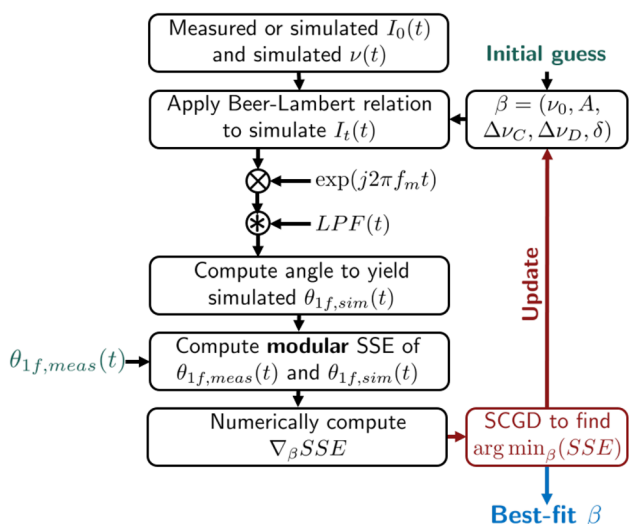
Fig. 3 Flowchart illustrating the WMS-θ_{1f} spectral fitting routine
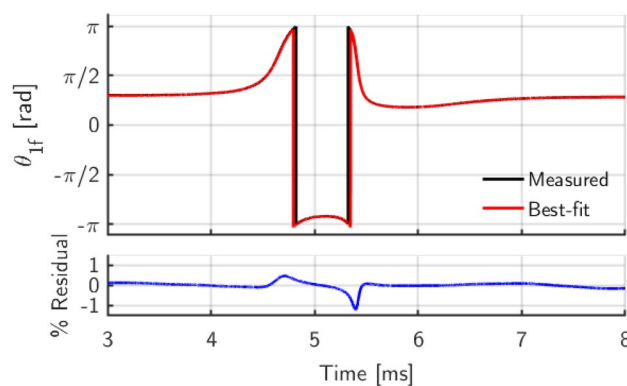

Fig. 4 Example WMS-θ_{1f} signal (black) for an optically thick absorbing gas medium. Without appropriately accounting for the phase discontinuity near $t = 4.75$ ms with a modified definition for sum-of-squared-errors, the WMS-θ_{1f} spectral fitting routine would not be able to converge onto the best-fit signal shown in red

with the simulated or previously measured $I_0(t)$ and $\nu(t)$ to calculate the simulated transmitted intensity $I_t(t)$ using Eq. 1. The resulting simulated $I_t(t)$ is then lock-in filtered to determine the simulated θ_{1f} signal ($\theta_{1f,\text{sim}}(t)$) using Eqs. 12 and 13. The background phase, δ, is a constant offset added to the simulated θ_{1f} to account for variations in the timing of $I_0(t)$ relative to the measured $I_t(t)$ caused by variations in the trigger point of a data acquisition system.

The sum-of-squared errors (SSE) between the simulated and measured $\theta_{1f}(t)$ signals is then computed. However, phase angles are modular (e.g. 0 and 2π are identical), which can lead to errors in calculating the true SSE without appropriate corrections. For example, $-3\pi/4$ and $3\pi/4$ are separated in phase space by only $\pi/2$, yet the standard definition of SSE would assume a separation of $3\pi/2$. Therefore, the typical definition of SSE needs to be modified to account for the modularity:

$$
\text{SSE} = \sum_t \{\min[|\theta_{1f,\text{meas}}(t) - \theta_{1f,\text{sim}}(t) + (2\pi, 0, -2\pi)|]\}^2.
\tag{14}
$$

By taking the minimum of $|\theta_{1f,\text{meas}}(t) - \theta_{1f,\text{sim}}(t)|$ offset by 2π, 0, or -2π, this expression ensures that only the true angular separation between $\theta_{1f,\text{meas}}(t)$ and $\theta_{1f,\text{sim}}(t)$ is used to compute SSE. This effect is illustrated in Fig. 4 for an optically thick θ_{1f} signal that exceeds $\theta_{1f} = \pi$ and wraps into $\theta_{1f} = -\pi$ near $t = 4.75$ ms. Without the modular SSE, the fitting routine would not be able to account for the apparent discontinuity in phase angles and converge onto correct values for the spectroscopic parameters.

The parameter vector, β, composed of the Voigt profile spectroscopic parameters and δ, is then numerically perturbed to compute (via one-sided finite differencing) the approximate gradient of the SSE with respect to β, $\nabla_\beta\text{SSE}$. Stochastic Polak–Ribiere conjugate gradient-descent (SCGD) [25] is then used to iteratively update β until SSE reaches a minimum. Note that this optimization scheme is different than the Levenberg–Marquardt algorithm [26, 27] commonly used in the literature to search for the best-fit β. Although the convergence rate for Levenberg–Marquardt is generally faster than SCGD, in practice, SCGD was observed to be more numerically stable at converging onto optimal values, especially for heavily distorted signals. Additionally, SCGD allows the user to arbitrarily specify the cost function for minimization rather than being restricted to SSE.

3 WMS-θ_{1f} signal distortion analysis and laser-tuning parameter optimization

With the theoretical basis and practical fitting guidelines for WMS-θ_{1f} signals established in the preceding section, we now analyze and optimize WMS-θ_{1f}-based sensors for measurements in harsh environments. Integral to this analysis are direct comparisons against the well-established WMS-$nf/1f$ and SDAS techniques used throughout the literature with the explicit goal of understanding the expected performance of WMS-θ_{1f} sensors for practical sensing applications.

It should be noted that the vast majority of TDLAS use cases involve the accurate determination of the mole fraction, temperature, and/or pressure of the absorbing species. All of these parameters directly factor into the integrated absorbance, A, as shown in Eq. 5. Hence, the current analysis focuses specifically on quantifying the impact of environmental distortions on the resulting uncertainty in the best-fit A. Though uncertainties in best-fit $\Delta\nu_C$, ν_0, and δ were not

evaluated, the methods used in this work can be generalized for such purposes.

3.1 Difficulties with the standard WMS optimization approach

The standard approach for optimizing the laser-tuning parameters of WMS-based sensors (referred to as the "standard optimization approach" or SOA) maximizes the expected peak WMS signal strength near the transition linecenter for a given measurement environment [8, 17, 18]. For example, the peak WMS-2f, -3f, and -4f signal responses occur when the modulation index, μ, is set to 2.2, 3.35, and 4.25, respectively, for a single absorption transition described by a Voigt profile. This scheme is intuitive because it theoretically maximizes the signal-to-noise ratio (SNR) of the WMS signals relative to background distortions in I_t from the measurement environment. Since the amplitude of the WMS harmonics responds in proportion to the integrated absorbance, measurement precision would be maximized at these optimal setpoints. For spectrally resolved scanned-WMS signals, however, additional optimization factors must be considered as illustrated below.

Figure 5 plots the peak-normalized linecenter signal responses for WMS-θ_{1f}, -2f/1f, -3f/1f, and -4f/1f as a function of μ for an example absorption transition described by a Voigt profile with peak absorbance = 0.063 and $\Delta\nu_C/\Delta\nu_D = 10$. Here, the response of WMS-θ_{1f} is defined as the phase difference between the maximum and minimum phases in a θ_{1f} signal. Like what was observed in Goldenstein et al. [16], the maximum signal responses for WMS-2f/1f, -3f/1f, and -4f/1f signals occur near $\mu = 1.1$, 1.6, and 1.9, respectively. In contrast, the maximum response for
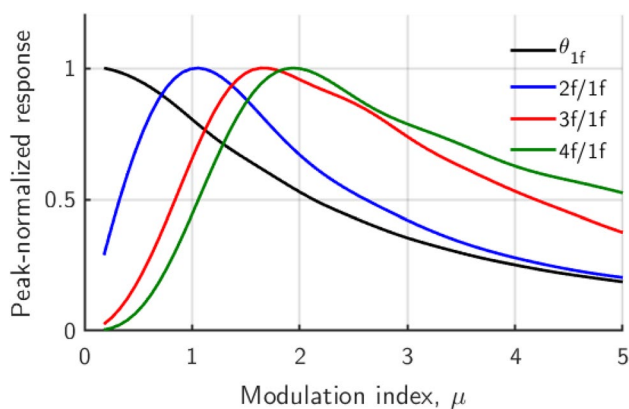
WMS-θ_{1f} occurs when $\mu \to 0$, a behavior first observed in Yang et al. [14]. This presents several inconsistencies and weaknesses in the SOA:

1. The modulation index, μ, can never be truly zero because $H_{k>0} = 0$ when $\mu = 0$ (see Eq. 11). As a result, based on Eq. 13, $\theta_{1f} = \text{const.}$ and does not respond to gas absorption.
2. Although the SOA maximizes the expected signal responses, it assumes that the noise amplitude is independent of laser-tuning parameters. It is not guaranteed that WMS signals are minimally sensitive to signal distortions within the measurement environment at the optimal values of μ in Fig. 5.
3. The Allan variance of measured CO_2 mole fractions in the static cell experiments using the WMS-θ_{1f} method presented in Yang et al. [14] decreased for all integration times with increasing μ, which is opposite to the expected trend based on Fig. 5.

These difficulties suggest that the SOA fails to account for additional complexities of spectrally resolved scanned-WMS signals and its interaction with environmental distortions. Thus, to address these complexities, a new analysis and optimization scheme that directly considers the combined effects of spectral fitting and environmental distortions is needed.

3.2 Additive and multiplicative signal distortions

We now consider the effects of additive (e.g. optical emission and offsets in the detection and digitization electronics chain) and multiplicative (e.g. non-absorption transmission losses from beam-steering or particulate matter occlusion) signal distortions on the accuracy of WMS-θ_{1f} and -nf/1f measurements. The current analysis specifically evaluates the effects of broadband distortion signatures with bandwidth on the order of the modulation frequency, f_m. This was done because it is well established both theoretically and experimentally that additive and multiplicative distortions with bandwidth less than $f_m/2$ can be corrected by WMS-nf/1f and WMS-θ_{1f} [18, 28]. These broadband distortions are often the dominant source of error for WMS-based measurements in harsh environments (see [12, 29], for example) and, therefore, deserve significant attention. It should be noted that a similar analysis was performed for SDAS and its comparison against the various WMS techniques is included in "Appendix" and summarized in Sect. 3.4.

Rather than mathematically modeling how these distortions affect measurement uncertainty, it is sufficient and significantly more efficient and illustrative to numerically compute measurement uncertainty by perturbing the ideal transmitted intensity, I_t, with simulated distortions from a target measurement environment. The frequency content and

Fig. 5 Peak-normalized signal responses for WMS-θ_{1f}, -2f/1f, -3f/1f, and -4f/1f as a function of modulation depth, μ for a single absorption transition with peak absorbance of 0.063 and $\Delta\nu_C/\Delta\nu_D = 10$. The simulation assumes $i_{m,1} \propto a_{m,1}$ similar to the behavior of real semiconductor lasers. Note that the optimal μ for maximum θ_{1f} signal response is 0

temporal behavior of these signal distortions can vary widely depending on the measurement environment and experimental hardware. Thus, to maximize the generality of the current analysis, $1/f$ random pink noise was used to simulate the additive ($\kappa(t)$) and multiplicative ($\rho(t)$) distortion time series, which may be constructed as follows:

$$\kappa(t) = \xi_\kappa \cdot \left[(1/f\text{-filter}) * \widetilde{\mathcal{N}_t(0,1)} \right], \tag{15}$$

$$\rho(t) = \exp\left[\xi_\rho \cdot (1/f\text{-filter}) * \widetilde{\mathcal{N}_t(0,1)} \right], \tag{16}$$

where ξ_κ and ξ_ρ are user-defined additive and multiplicative distortion amplitudes, respectively, and $\mathcal{N}_t(0,1)$ denotes a Gaussian white noise time series constructed by randomly sampling a normal distribution with zero mean and standard deviation $= 1$. The $1/f$-filter transfer function, $G_{1/f}(f)$, has zero phase with frequency-dependent gain defined as follows:

$$\left| G_{1/f}(f) \right| = \frac{1}{1 + \left(\frac{f}{f_{1/2}} \right)^p}, \tag{17}$$

where $f_{1/2}$ is the frequency "elbow" corresponding to $G_{1/f} = 1/2$ and kept at $f_{1/2} = 0.1 f_m$ throughout this work to ensure that $G_{1/f}$ asymptotically decays as a function of $1/f^p$ at the harmonics of the modulation frequency. p is the frequency roll-off exponent, which sets the relative impact of the distortion signals on the modulation harmonics. $G_{1/f}$ is plotted as a function of f/f_m in Fig. 6 (log–log space) for various values of p with important frequencies labeled. Note that the choice of ξ_κ and ξ_ρ are inconsequential to the conclusions drawn from this work as long as they are small relative to $\overline{I_0}$ (to prevent exceedingly poor spectral fits) and kept constant when comparing the results of the various
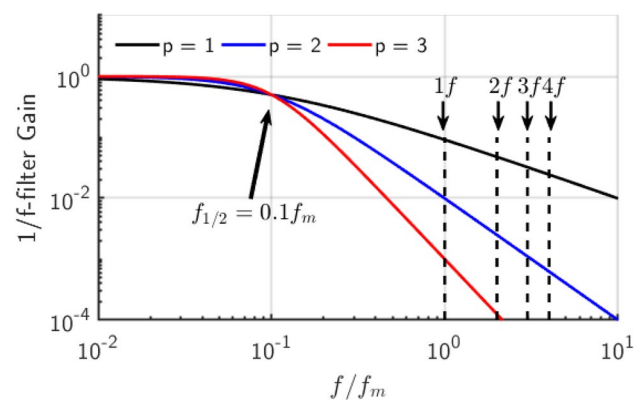

Fig. 6 Gain as a function of frequency normalized by the modulation frequency ((log–log space) for various values of the roll-off exponent, p, for the $1/f$ filter used to generate the stochastic additive and multiplicative distortion time series in Eqs. 15 and 16

WMS techniques against each other. The roll-off exponent, p, however, is an important parameter and is the subject of Sect. 3.2.3. $\kappa(t)$ and $\rho(t)$ were then used to distort $I_t(t)$ to yield the distorted transmitted intensity, $\widetilde{I_t(t)}$, as follows:

$$\widetilde{I_t(t)} = \rho(t) \cdot I_t(t) + \kappa(t). \tag{18}$$

$\widetilde{I_t(t)}$ was then passed through the lock-in filter and angle calculation operations (Eqs. 12 and 13) to determine the distorted θ_{1f} signal, $\widetilde{\theta_{1f}}$. An example of the effects of such a distortion on a TDLAS experiment for an absorbing gas described by a single Voigt profile is shown in Fig. 7 for the transmitted intensity (top panel) and best-fit θ_{1f} signal and residual (middle and bottom panel) assuming $\xi_\kappa = 0.1\overline{I_0}$, $\xi_\rho = 0.1$, and $p = 1$. Note that the distortion introduced a 4.96% error in the best-fit integrated absorbance relative to the known value.

The WMS-θ_{1f} and WMS-nf/$1f$ spectral fitting routines were then used to compute best-fit values of A for the distorted signal, denoted as $\widetilde{A}$, for a large collection (size N) of randomly distorted $\widetilde{I_t(t)}$. A sample-averaged error in the best-fit integrated absorbance can then computed as follows:
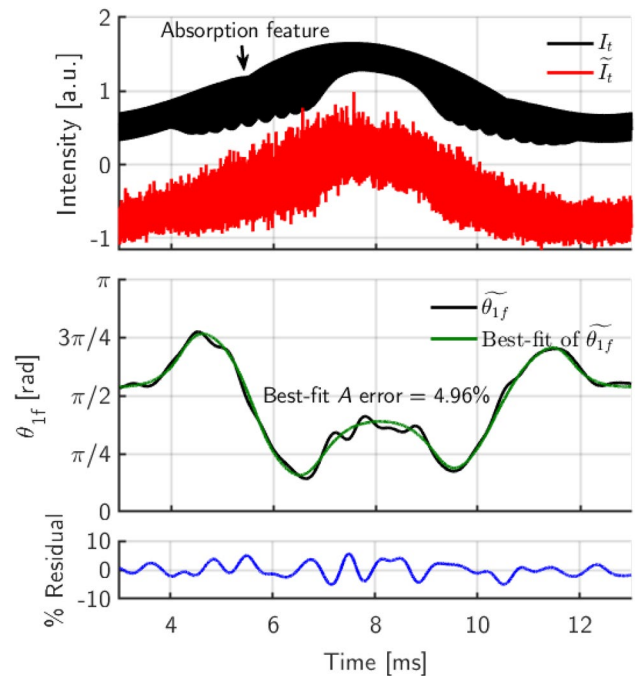

Fig. 7 Example effect of $1/f$ additive and multiplicative distortions on the transmitted intensity (top panel) and the resulting best-fit WMS-θ_{1f} signal and residuals (middle and bottom panels) for an absorbing gas described by a single Voigt profile. The distortion introduced a 4.96% error in the best-fit integrated absorbance relative to the known value

$$\epsilon_A = \frac{1}{N} \sum_{k=1}^{N} \left| \frac{\widetilde{A}_k - A_{\text{known}}}{A_{\text{known}}} \right|, \tag{19}$$

where A_{known} is the user-defined value for A used in the simulated absorption spectrum. N was set to be 200 for the results presented in this article, which was observed to be sufficient to converge onto a statistically stable value for ϵ_A. ϵ_A can be interpreted as the true figure of merit for optimizing the laser-tuning parameters of any scanned-WMS technique with respect to additive and multiplicative distortions in the environment. Rather than optimizing the expected WMS response just near linecenter, ϵ_A explicitly evaluates the combined effects of environmental distortions, laser-tuning parameters, and the spectral fitting routine on the results of a scanned-WMS measurement. Laser-tuning parameters should thus be selected such that ϵ_A is at a global minimum.

3.2.1 IM–FM phase delay optimization

As noted in Sect. 2.2, WMS-θ_{1f} signals are sensitive to the linear phase delay between the intensity modulation (IM, described by the m-component of Eq. 6) and the frequency modulation (FM, described by the m-component of Eq. 7) waveforms, defined here as $\psi_{\text{m},1} - \phi_{\text{m},1}$. In particular, for operating conditions where $\text{mod}(\psi_{\text{m},1} - \phi_{\text{m},1}, \pi) = 0$, the WMS-$\theta_{1f}$ signal is insensitive to gas absorption and cannot be used for spectroscopic measurement. Consequently, ϵ_A for WMS-θ_{1f} signals is expected to depend strongly on the IM–FM phase delay.

Figure 8 plots ϵ_A for WMS-θ_{1f} as a function of the IM–FM phase delay for various modulation indices and at a fixed scan index, σ, equal to 9. All simulations assume fixed laser tuning, distortion, and absorption spectrum parameters as listed in Table 1. f_{cutoff} here represents the cutoff frequency of the brick-wall low-pass filter used to compute the WMS harmonics. The range of IM–FM phase delays considered here was $\pi \rightarrow 3\pi/2$ corresponding to the physical limits of injection current-tuned lasers (based on thermal lag arguments discussed in Sect. 2.2), with π corresponding to $f_{\text{m}} \rightarrow 0$ and $3\pi/2$ corresponding to $f_{\text{m}} \rightarrow \infty$.

As can be seen from Fig. 8, the minimum sample-averaged error in the best-fit integrated absorbance corresponds to an IM–FM phase delay of $3\pi/2$ and its optimal
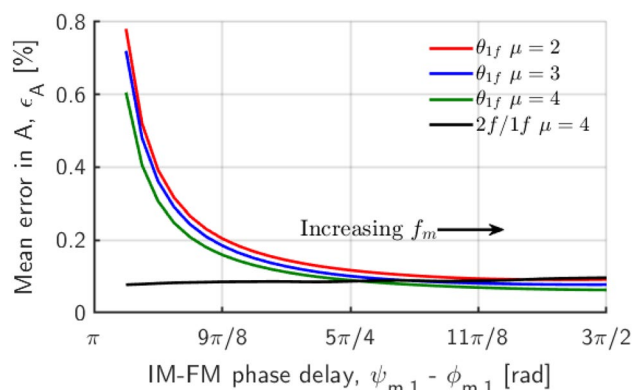

Fig. 8 Sample-averaged error in the best-fit integrated absorbance as measured with a least-squares best-fit of distorted WMS-θ_{1f} signals plotted as a function of the intensity-optical frequency modulation phase delay for various modulation indices (red, blue, and green). Note that for all modulation indices, the minimum error occurs when $\psi_{\text{m},1} - \phi_{\text{m},1} = 3\pi/2$, which corresponds to the IM–FM phase delay at infinite modulation frequency for injection current-tuned lasers. Mean error rate of distorted WMS-$2f/1f$ signals is shown in black for $\mu = 4$ to demonstrate the near independence of WMS-$nf/1f$ measurement accuracy on the IM–FM phase delay

positioning is independent of the modulation index. More generally, the $3\pi/2$ optimality criterion was verified to be independent of the characteristics of the distortion environment and laser-tuning parameters (data not shown for brevity). This demonstrates that it is beneficial to modulate the laser at as high of a frequency as possible to maximize the IM–FM phase delay and thus desensitize the sensor to additive and multiplicative distortions. However, above a phase delay of approximately $5\pi/4$, ϵ_A quickly asymptotes towards the minimum value and becomes nearly independent of the IM–FM phase delay; hence, there are diminishing returns for modulating at increasingly high frequencies. For the example laser used to generate Fig. 2, modulation frequencies above 200 kHz correspond to IM–FM phase delays that are in the asymptotic region of Fig. 8.

For WMS-$nf/1f$ measurements, ϵ_A is expected to be nearly independent of the IM–FM phase delay because the analytical expressions for $|R_{nf}/R_{1f}|$ are weakly dependent on $\psi_{\text{m},1} - \phi_{\text{m},1}$ [17]. This is demonstrated in the black curve in Fig. 8, which plots ϵ_A for WMS-$2f/1f$ measurements as a function of $\psi_{\text{m},1} - \phi_{\text{m},1}$ for $\mu = 4$ and $\sigma = 9$. As can be seen,

Table 1 Laser tuning, distortion, and absorption spectrum parameters used to numerically compute ϵ_A in Figs. 8, 9, and 10

f_{m}	f_{s}	ξ_ρ	ξ_κ	$f_{1/2}$	σ
100 kHz	1 kHz	0.01	$0.01\overline{I_0}$	$0.1f_{\text{m}}$	9
f_{cutoff}	p	A	$\Delta\nu_{\text{C}}$	$\Delta\nu_{\text{D}}$	ν_0
$10f_{\text{s}}$	1	0.05 cm^{-1}	0.1 cm^{-1}	0.01 cm^{-1}	$\overline{\nu}$

ϵ_A remains nearly constant as a function of $\psi_{m,1} - \phi_{m,1}$. In practice, the variation of $\psi_{m,1} - \phi_{m,1}$ with modulation frequency for specific lasers is strongly dependent on the laser architecture and intrinsic properties. For applications where the IM–FM phase delay cannot reach the asymptotic region of Fig. 8 with phase delay greater than $5\pi/4$ (e.g. for systems that are unable to modulate the lasers at sufficiently high frequencies or for lasers with exceptionally low thermal mass), WMS-nf/1f may be the preferred measurement technique relative to WMS-θ_{1f} since its accuracy is nearly independent of $\psi_{m,1} - \phi_{m,1}$.

3.2.2 Scan and modulation index optimization for $p = 1$

We now optimize the scan and modulation indices of the various WMS methods under the influence of additive and multiplicative distortions for the specific case where the frequency roll-off exponent (p in Eq. 17) equals unity. This value of p was chosen because such distortion signatures are commonly found in nature as the limiting statistical distribution of diverse stochastic processes [30]. Despite this choice, the methods used in this work can be used to assess the performance of WMS sensors for arbitrary values of p.

Similar to the IM–FM phase delay optimization scheme, ϵ_A can be evaluated for a variety of scan and modulation indices (σ and μ, respectively) for a given absorption spectrum and distortion environment to determine optimal values for μ and σ, denoted as μ^* and σ^*, respectively. We first restrict the analysis specifically on the impact of μ while keeping σ constant, similar to what is considered in the standard optimization approach. The results are shown in Fig. 9, which plots ϵ_A as a function of μ for WMS-θ_{1f} and WMS-nf/1f with $n \in [2, 3, 4]$. All simulations assume the same low-frequency scan, pink-noise, and gas absorption parameters listed in Table 1. Additionally, laser-tuning parameters in Eqs. 6 and

Fig. 9 Sample-averaged error in the best-fit integrated absorbance as a function of modulation index for WMS-θ_{1f} and various WMS-nf/1f signals distorted by random 1/f additive and multiplicative noise

7 used to simulate the results were experimentally determined values from a DFB-TDL operating near 2.017 μm (Nanoplus) with $f_m = 100$ kHz and $f_s = 1$ kHz. For the θ_{1f} results, $\psi_{m,1} - \phi_{m,1}$ was measured to be 1.36π at $f_m = 100$ kHz, which is within the asymptotic region of Fig. 8.

Several trends can be observed and conclusions drawn from Fig. 9:

1. Regardless of μ, WMS-θ_{1f} exhibits improved measurement accuracy over the various WMS-nf/1f methods. In general, the accuracy of WMS-nf/1f worsens as n increases. This trend agrees with the superior Allan variance of the WMS-θ_{1f} or WMS-R_{1f}/Y_{1f} measurements shown in Yang et al. [14] and Upadhyay et al. [15] when compared to concurrent WMS-2f/1f measurements.

2. ϵ_A for θ_{1f} measurements decreases as a function of μ. This behavior contrasts with the SOA of WMS-θ_{1f} shown in black in Fig. 5, where ϵ_A for WMS-θ_{1f} signals are expected to increase as a function of μ due to the lower θ_{1f} signals response at higher values of μ. Likewise for the various WMS-nf/1f methods, besides local minima near $\mu = 3$, 4.5, and 5.3 for WMS-2f/1f, -3f/1f, and -4f/1f, respectively, ϵ_A decreases as a function of μ in general.

Given the unexpected behavior of ϵ_A versus μ compared to the expectation from the standard optimization approach, it is natural to question whether the choice of σ has an influence on ϵ_A. Past researchers provided heuristic σ-selection guidelines [16] that only suggest selecting a sufficiently large σ to spectrally resolve the WMS-nf/1f signal lobes but do not assess how σ impacts measurement accuracy. Figure 10a shows the numerically calculated ϵ_A for WMS-θ_{1f} color-mapped onto a matrix of μ–σ pairs, with black and dark blue colors representing better measurement accuracy. Note the existence of multiple valleys of optimal μ and σ with troughs best described by the lines $\sigma = 1.05\mu + 1.17$ (labeled as "Valley 1") and $\sigma = 0.93\mu - 0.73$ ("Valley 2"). μ–σ pairs along these troughs may be considered as "good choices" for minimizing θ_{1f} sensitivity to additive and multiplicative signal distortions with roll-off exponent, p, equal to 1. The global minimum for ϵ_A exists within Valley 2 at $(\mu^*, \sigma^*) = (6.4, 5.2)$. However, since these μ and σ values are relatively large and difficult to achieve except for absorption spectra with small linewidths (e.g. gases at low pressures) or exceptionally wide-tuning lasers, it is more practically relevant to consider the behavior of ϵ_A at lower μ and σ values. Figure 10b shows a cutaway of the region between $\mu = 2 \rightarrow 5$ and $\sigma = 3 \rightarrow 7$ bisected by Valley 1. It can be seen that there exists a $(\mu^*, \sigma^*) = (4.5, 5.6)$ pair that locally minimizes ϵ_A with more reasonably achievable scan and modulation depths. For practical environments where laser-tuning range relative to absorption linewidth is limited,
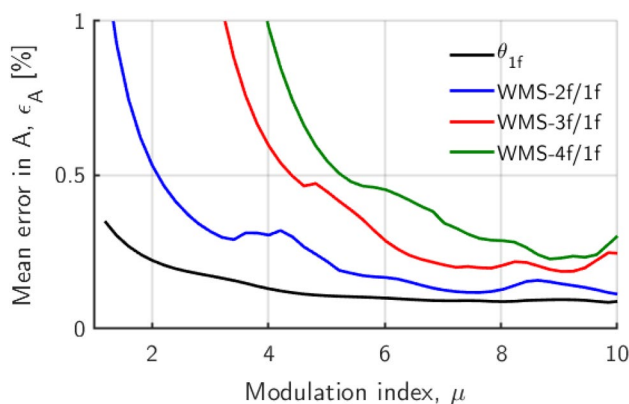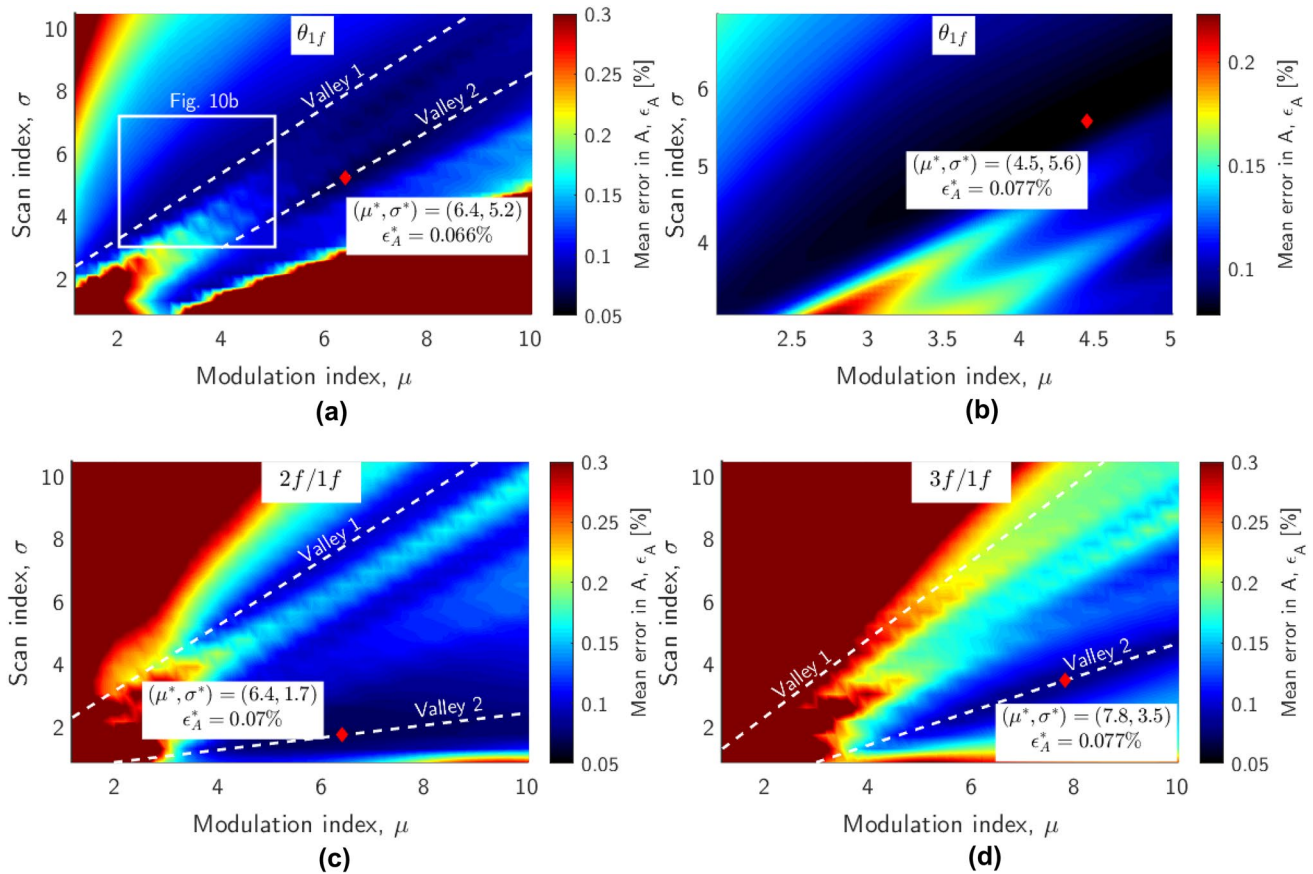
Fig. 10 Sample-averaged error in the best-fit integrated absorbance color-mapped onto a matrix of scan and modulation index pairs for **a, b** WMS-θ_{1f}, **c** 2f/1f, and **d** 3f/1f signals distorted by random 1/f addi-tive and multiplicative noise with $p = 1$. "Valleys" of optimal μ–σ pairs are highlighted in dotted white lines. Global optima are marked with red diamonds

it is possible to select slightly suboptimal μ–σ pairs along Valley 1 such as (2.5, 3.8) without significant loss in accuracy. Repeated simulations indicated that the μ–σ trough equation and the optimal (μ^*, σ^*) pair were insensitive to IM–FM phase delays, ξ_ρ, ξ_κ, and peak absorbances at a constant $p = 1$ (results not shown for brevity).

Similar analyses can be performed for distorted WMS-2f/1f and -3f/1f signals, whose results are shown in Fig. 10c, d, respectively. Note that the ϵ_A color-scales for these two figures were kept consistent with the color scale used in Fig. 10a; hence, ϵ_A values exceeding 0.3% were displayed as uniformly dark red. Several conclusions can be drawn from comparing ϵ_A among the different WMS techniques.

1. Like in Fig. 10a, there exist multiple valleys of optimal μ and σ. For WMS-2f/1f, the troughs of these valleys are described by the equations $\sigma = 1.04\mu + 1.08$ and $\sigma = 0.2\mu + 0.5$ for Valleys 1 and 2, respectively. The global optimum lies within Valley 2 at $(\mu^*, \sigma^*) = (6.4, 1.7)$. For WMS-3f/1f, the troughs are described by $\sigma = 1.24\mu - 0.16$ and $\sigma = 0.52\mu - 0.75$ for

Valleys 1 and 2, respectively, with the global optimum lying in Valley 2 at $(\mu^*, \sigma^*) = (7.8, 3.5)$.

2. Although the global minima in ϵ_A for WMS-2f/1f and -3f/1f are comparable to the minimum for θ_{1f}, the WMS-nf/1f strategies generally do not perform as well as θ_{1f} at low modulation and scan indices. In practical harsh environments with pronounced lineshape broadening effects, lasers are often incapable of reaching the μ and σ needed to reach the optimal valleys of the WMS-nf/1f techniques, suggesting that WMS-θ_{1f} would be the preferred sensing technique for distortion-heavy environments or where maximum measurement rate is important.

It is difficult to identify precise reasons for the trends observed in Fig. 10 in the absence of a mathematical model. It is, however, possible to elucidate qualitative intuitions that can explain key features. For example, to explain the existence of the valleys of optimal μ–σ pairs, we propose the following line of reasoning.
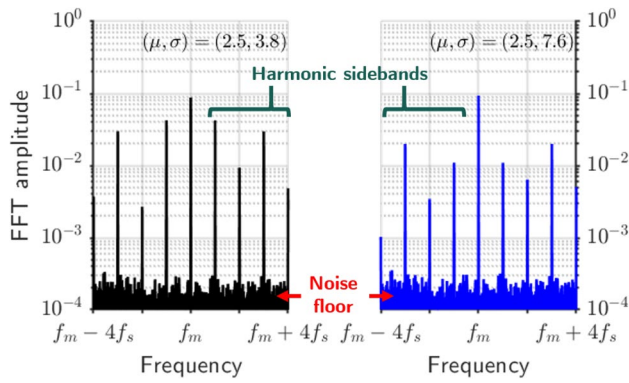
Fig. 11 Frequency spectrum of the transmitted intensity of a scanned-wavelength WMS experiment near the first harmonic with (left panel) $(\mu, \sigma) = (2.5, 3.8)$ and (right panel) σ doubled to 7.6 while keeping μ constant. Note the weakening of the harmonic sidebands relative to the noise floor with increasing σ

Fig. 12 Simulated WMS-$2f$/$1f$ signals over a single up-scan for a range of μ–σ pairs obeying the two μ–σ valley trough equations observed in Fig. 10c

1. Assuming a constant μ, for low values of σ, the laser does not sample over a sufficient fraction of the absorption spectrum during each scan cycle, leading to an insufficiently constrained fitting problem that leads to large errors. Specifically, at low values of σ, A and $\Delta\nu_C$ become less distinct in their effects on simulated WMS signals, resulting in best-fit A that are susceptible to signal distortions. This explains the generally high ϵ_A values at low σ in Fig. 10.

2. Conversely, for exceedingly large values of σ, the laser tunes across the absorption spectrum very quickly during each scan cycle, thus requiring larger amplitudes at high sideband frequencies to represent the signals. Figure 11 illustrates this effect for the sidebands surrounding the first harmonic of the transmitted intensity of a WMS experiment. As can be seen, when σ is doubled from 3.8 (left) to 7.6 (right) at constant $\mu = 2.5$, the harmonic sidebands become weaker on average and more widely distributed in frequency (not visible here but demonstrated in Fig. 7 of [17]), resulting in lower average SNR in the sidebands. Since these sidebands encode information needed for WMS spectral fitting, the lower SNR is expected to contribute to greater ϵ_A.

3. As a result of the previous two arguments, for each μ, a certain optimal σ exists that is both large enough to sufficiently constrain the WMS spectral fitting routine and small enough to maintain good SNR in the harmonic sidebands relative to the noise floor.

4. In general, as μ increases at a constant σ, the width of the WMS signal lobes in the time-domain increases. This requires a corresponding increase in the minimum σ needed to fully resolve the WMS signal lobes and sufficiently constrain the WMS spectral fitting routine. Together with the preceding observations, the net result
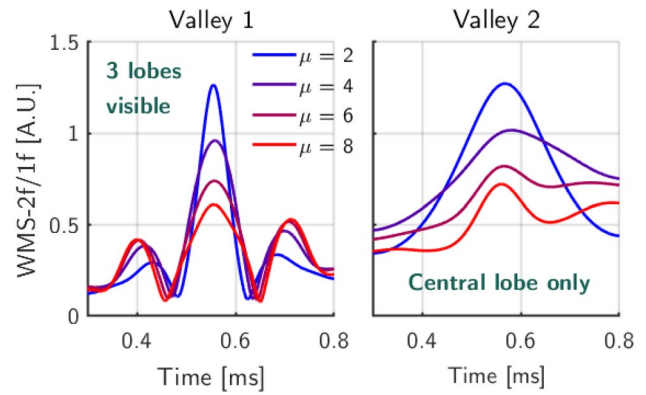
is the existence of valleys of optimal μ–σ pairs exhibiting positive slope as evidenced in Fig. 10.

It is also possible to qualitatively explain the existence of multiple optimal μ–σ valleys in Fig. 10. Figure 12 plots simulated WMS-$2f$/$1f$ signals over a single up-scan for a range of μ–σ pairs evaluated along the optimal trough equations describing Valley 1 (left) and Valley 2 (right) observed in Fig. 10c. As can be seen, WMS-$2f$/$1f$ signals along Valley 1 show the three canonical WMS-$2f$/$1f$ lobes while signals along Valley 2 show only the central lobe near transition linecenter. This observation applies equally to WMS-θ_{1f} and WMS-$3f$/$1f$ signals along their respective μ–σ valleys (not shown). It is, therefore, reasonable to conclude that the various μ–σ trough equations optimize the laser tuning parameters for different numbers of WMS lobes observed in the measured signal.

3.2.3 Dependence on the frequency roll-off exponent, p

Section 3.2.2 demonstrated that WMS-θ_{1f} measurements are generally less sensitive to additive and multiplicative distortions assuming that the frequency content of the distortions rolls off as a function of $1/f$. However, as the frequency roll-off exponent, p, increases, the impact of the distortions on the $n > 1$ harmonics of f_m become weaker relative to the impact on the first harmonic. Therefore, it is expected that there exists some value of p at which WMS-nf/$1f$ measurements are more accurate than WMS-θ_{1f}. Similarly, as $p \to 0$, the distortion signal approaches white noise and equally impacts the signals of all WMS harmonics. Since most of the absorption-induced frequency content in $I_t(t)$ is concentrated near the first harmonic, it is expected that WMS-θ_{1f} will perform better than nf/$1f$ at low values of p.

Figure 13 confirms the preceding arguments. Here, the accuracy of the various WMS techniques were evaluated
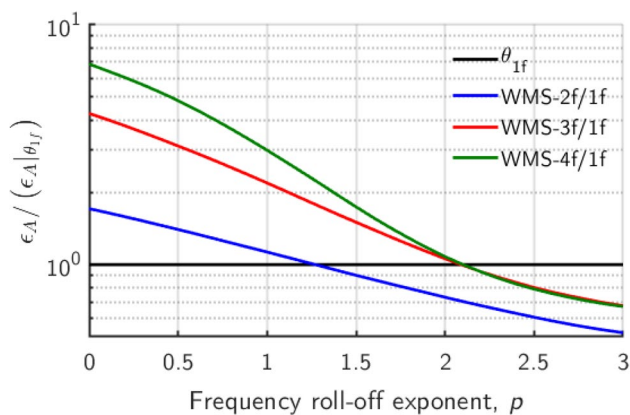
Fig. 13 Sample-averaged error in the best-fit integrated absorbance, ϵ_A, as a function of the frequency roll-off exponent, p, for WMS-θ_{1f} and various WMS-nf/1f signals distorted by random $1/f^p$ additive and multiplicative noise. Results were normalized by the error in WMS-θ_{1f}, $\epsilon_A|_{\theta_{1f}}$, at each value of p

as a function of p assuming the same simulated absorption spectrum and distortion amplitudes listed in Table 1. σ and μ for each WMS technique were set to the optimal values as calculated for $p = 1$ using the methods in Sect. 3.2.2. The resulting ϵ_A values were then normalized by the calculated ϵ_A for WMS-θ_{1f} and plotted in Fig. 13 as a function of p. As can be seen, below $p = 1.25$, WMS-θ_{1f} performs better than WMS-nf/1f, consistent with the $p = 1$ results in Sect. 3.2.2. Above $p = 1.25$, the greater roll-off exponent desensitizes WMS-2f/1f measurements to the frequency content of the distortions, allowing second harmonic detection to perform better than WMS-θ_{1f}. WMS-3f/1f and -4f/1f never perform better than -2f/1f and do not exceed θ_{1f} performance until $p > 2.1$. It should be noted that the specific intersection points in the roll-off exponent shown in Fig. 13 are specific to the selected laser-tuning parameters and may vary as a function of μ, σ, and distortion amplitudes. However, the general trends shown in Fig. 13 are representative of all conditions.

In practice, the true value of p depends strongly on the frequency-domain characteristics of the distortion sources within the measurement environment. For example, experiments in non-isothermal jet flows [31] show that the density fluctuation spectrum (and by extension, the beam-steering spectrum) within the inertial subrange of the potential core decays with $p = 3.4$, which is well outside the region in Fig. 13 where WMS-θ_{1f} would be the preferred measurement technique. Conversely, TDLAS distortions within the combustion annulus of a rotating detonation engine—a representative environment where additive and multiplicative signal distortions are strong and diverse in source—were found to exhibit a $p = 1.1$ roll-off exponent [32], indicating that WMS-θ_{1f} may be the preferred measurement technique in such an environment. As a result, it is important for sensor

designers to assess the expected frequency-dependence of the distortion characteristics within a measurement environment to select an appropriate WMS detection scheme. Practically, one can characterize the additive and multiplicative distortion signatures within a measurement environment by measuring the transmitted intensity of a laser operating at constant intensity and at a non-absorbing wavelength. The information gathered from these initial experiments can guide the selection of the optimal WMS technique and laser-tuning parameters.

3.3 Wavelength-dependent signal distortions

In some environments, wavelength-dependent distortions resulting from étalon cavities can be difficult to avoid and are often major sources of uncertainty in practical TDLAS experiments. Additionally, these distortions often vary with time due to vibration- or temperature-induced changes in alignment and can significantly impact the long-term stability of laser-based sensors. Therefore, it is important to assess the impact of these distortions on the accuracy of WMS-based measurements. A comparison with SDAS-based sensors was also performed and is included in "Appendix" and summarized in Sect. 3.4.

Étalon-induced wavelength-dependent distortions generally manifest as periodic offsets in α_ν. To first order, these offsets may be approximated as sinusoidal distortions to the spectral absorbance with some free spectral range, T_D (cm^{-1}), and peak offset, δ_ν (cm^{-1}), relative to the transition linecenter:

$$\widetilde{\alpha}_\nu = \alpha_\nu + \xi_{\text{etln}} \cos\left(\frac{2\pi}{T_D}\left(\nu - \left(\nu_0 + \delta_\nu\right)\right)\right), \qquad (20)$$

where $\widetilde{\alpha}_\nu$ is the distorted spectral absorbance and ξ_{etln} is the étalon distortion amplitude. $\widetilde{\alpha}_\nu$ was then used to simulate a distorted I_t, which was spectrally fitted to determine the best-fit integrated absorbance, $\widetilde{A}$. An example of this distortion and its effect on the best-fit WMS-θ_{1f} signal is shown in Fig. 14 for an absorption spectrum described by $(A, \Delta\nu_C, \Delta\nu_D, \widetilde{\nu}) = (0.05, 0.1, 0.01, \overline{\nu})$ distorted with $\xi_{\text{etln}} = 0.1\alpha_{\max}$, $\delta_\nu = 0$, and $T_D = 0.4$ cm^{-1}. μ and σ for this example were set at 3.64 and 5.45, respectively. As can be seen, the wavelength-dependent distortion to the absorption spectrum introduced a 4.26% error in the best-fit integrated absorbance relative to the true value.

The error of the distorted best-fit integrated absorbance depends, in general, on T_D, $a_{m,1}$, $a_{s,1}$, FWHM of the absorption transition, ξ_{etln}, and δ_ν. To simplify the analysis, $a_{s,1}$ and ξ_{etln} were kept constant and T_D was nondimensionalized with $a_{m,1}$ to form $\eta = T_D/(2a_{m,1})$, identical to the scheme in [16]. Like the definition for ϵ_A, we similarly define an average error in the integrated absorbance due to
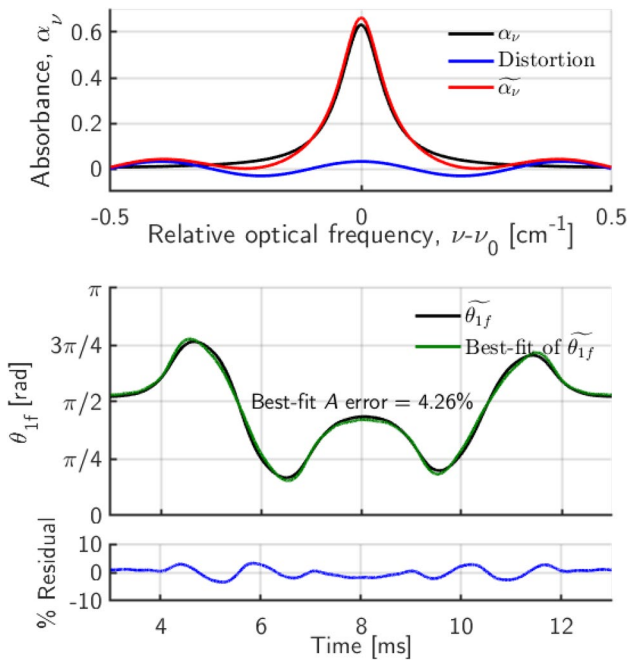
Fig. 14 Example effect of wavelength-dependent distortion on the spectral absorbance (top panel) and the resulting best-fit WMS-θ_{1f} signal and residuals (middle and bottom panel) for an absorbing gas described by a single Voigt profile. The distortion introduced a 4.26% error in the best-fit integrated absorbance relative to the true value

wavelength-dependent distortions, $\epsilon_{A,\text{etln}}$, for a given η and μ pair as follows:

$$\epsilon_{A,\text{etln}} = \frac{1}{N} \sum_{k=1}^{N} \left| \frac{\widetilde{A}(\delta_\nu = kT_D/N) - A_{\text{known}}}{A_{\text{known}}} \right|, \tag{21}$$

where N covers a range of individual δ_ν used for computing the average (100 was used in this work, sufficient to converge

onto stable values of $\epsilon_{A,\text{etln}}$). This analysis extends on the methods shown in Goldenstein et al. [16]. Specifically, this analysis computes the étalon-induced error in the best-fit integrated absorbance rather than just the sum-of-squared-errors in the WMS-nf/1f signal. In addition, this analysis extends the assessment to the full range of δ_ν, supplementing the work of [16] at just $\delta_\nu = 0$.

Figure 15 shows how $\epsilon_{A,\text{etln}}$ varies as a function of η for various μ for (a) WMS-θ_{1f} and (b) -2f/1f. Results are shown for a single Voigt profile described by $(A, \Delta\nu_C, \Delta\nu_D, \nu_0) = (0.05, 0.1, 0.01, \overline{\nu})$. σ and ξ_{etln} were set at 3.8 and 1% of the peak absorbance, respectively. Again, several trends can be observed from these results.

1. Similar to the observations in [16], $\epsilon_{A,\text{etln}}$ approaches zero when η approaches zero or infinity for all of the WMS techniques considered here. Also, $\epsilon_{A,\text{etln}}$ decreases in general with increasing μ.
2. The primary error band, representing the qualitative range of η in which $\epsilon_{A,\text{etln}}$ is greatest, is highlighted with black arrows in Fig. 15. As can be seen for WMS-θ_{1f} (Fig. 15a), the primary error band is wider in η than for WMS-2f/1f (Fig. 15b). However, the maximum errors for θ_{1f} within this band are less than the maximum errors for WMS-2f/1f. Additionally, θ_{1f} is more forgiving for distortions with small η (e.g. low free-spectral range étalons in the measurement environment) than WMS-2f/1f.
3. Results for higher harmonic WMS-nf/1f signals (e.g. WMS-3f/1f or -4f/1f, not shown here for brevity) indicate that the width of the primary error bands decreases with increasing n. However, $\epsilon_{A,\text{etln}}$ within the primary error band worsens with increasing n, indicating less forgiveness at higher detection harmonics for wavelength-dependent distortions with sub-optimal η.
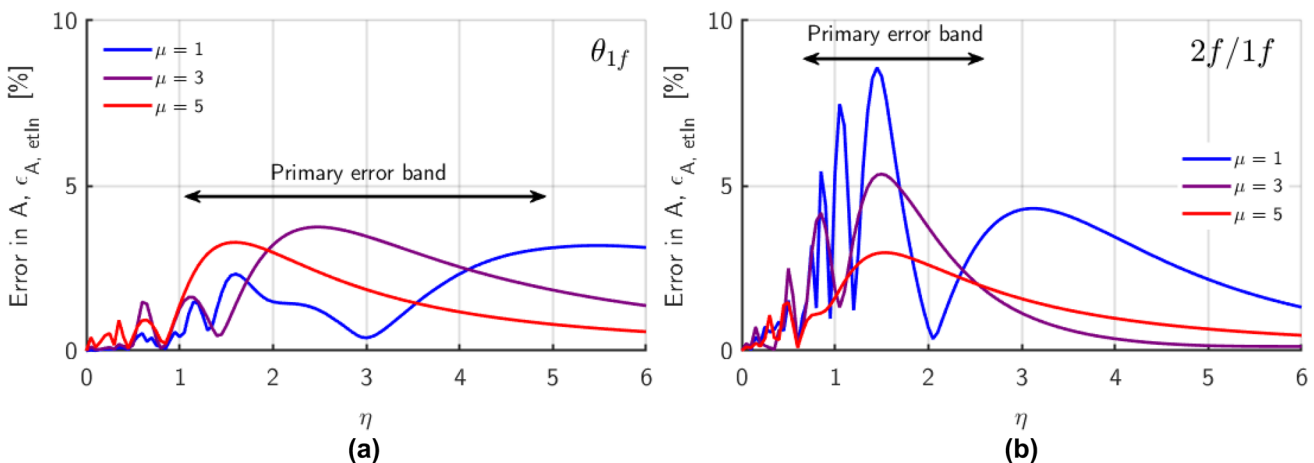

Fig. 15 Wavelength-dependent-distortion-induced errors in the best-fit integrated absorbance for **a** WMS-θ_{1f} and **b** -2f/1f. Distortion amplitude was 1% of the peak absorbance. Each curve represents a different value of modulation index

From these observations, we can conclude that WMS-θ_{1f} qualitatively performs just as well as typical WMS-$nf/1f$ methods under wavelength-dependent distortions. For some low-η measurement environments, WMS-θ_{1f} may even be the preferred measurement technique for maximum accuracy in the best-fit integrated absorbance. It should be noted that the results for optimizing WMS-based sensors against étalon noise may conflict with the optimization criteria for additive and multiplicative distortions discussed in Sect. 3.2. The authors again emphasize the need for sensor designers to appropriately characterize and assess the relative impact of the various sources of signal distortion in the measurement environment to select optimal laser tuning parameters.

3.4 Comparisons with scanned-wavelength direct absorption spectroscopy

Scanned-wavelength direct-absorption spectroscopy (SDAS) is a TDLAS technique where the laser source is periodically wavelength-tuned across an absorption transition. The measured transmitted intensity is used to directly calculate the absorption spectrum via Eq. 1, which can be fitted with absorption lineshapes to infer spectroscopic parameters not unlike the spectral fitting strategy in Sect. 2.3. Due to its simplicity in implementation and ease of real-time data visualization and troubleshooting as compared to WMS-based techniques, SDAS is, in general, the most widely used TDLAS sensing technique. As a result, there is considerable need to understand and quantify the relative performance of SDAS and WMS to justify the added complexity and overhead needed to implement WMS-based strategies. Fortunately, the analysis techniques described in the preceding sections can be generalized to SDAS, thereby allowing direct comparisons between SDAS and WMS.

Details related to the SDAS signal distortion analysis may be found in "Appendix". Key findings are summarized below.

1. There exists an optimal modulation index, $\mu^* = 5.6$, that minimizes ϵ_A for SDAS measurements when subjected to stochastic additive and multiplicative noise (see Fig. 22). To be consistent with the conventions used for WMS, modulation index for SDAS is defined as the ratio between the optical frequency scanning range to the half-width half-maximum of the absorption feature.

2. When subjected to the identical $p = 1$ additive and multiplicative distortions as used in Sect. 3.2.2, SDAS was found to perform significantly worse than the various WMS-based sensors (see Fig. 22a). This agrees with intuition because the frequency content of the distortions are concentrated at low frequencies near the harmonics of the SDAS measurements. Since SDAS does not filter

or correct for these distortions, it is expected that the performance of SDAS will be more heavily impacted.

3. However, for $p = 0$ additive and multiplicative distortions (i.e. white noise) where the distortions equally impact the SDAS and WMS harmonics, SDAS was found to perform as well as WMS-θ_{1f} and significantly better than either WMS-$2f/1f$ or $-3f/1f$ (see Fig. 22b). This suggests that, for certain environments with distortion characteristics that exhibit a roll-off exponent near zero (e.g. for quiescent environments where electronics noise is dominant), it may be detrimental to use WMS instead of SDAS in terms of sensor accuracy.

4. It is important to note that the intensity normalization and lock-in filtering operations inherent in WMS-based strategies are able to correct additive and multiplicative distortions with bandwidth below $f_m/2$. Since SDAS cannot intrinsically correct for these low-frequency distortions, for applications where strong, pure-tone oscillations are expected (e.g. for in situ monitoring of turbomachinery), SDAS measurement accuracy can be significantly worse than WMS measurement accuracy (see Fig. 23).

5. The accuracy of SDAS sensors is more strongly affected by short-period étalons (see Fig. 24), which is opposite the behavior of WMS-θ_{1f} sensors as demonstrated in Fig. 15a. This suggests that, for environments where wavelength-dependent distortions are the dominant source of measurement uncertainty, there are distinct ranges of η at which either WMS-θ_{1f} or SDAS is the preferred measurement technique.

These findings show that SDAS is not always the inferior measurement technique when compared to WMS. This again reinforces the need to characterize the expected distortion environment for a target application and to use the analysis techniques introduced in this work in order to select the optimal sensing strategy and laser tuning parameters.

4 Experimental validation and demonstration

Two sets of experiments were performed both to validate the simulation-based results shown in Sect. 3 (using a static gas cell) and to provide a demonstration of the utility of WMS-θ_{1f} for practical diagnostics (using a methane-air flame).

4.1 CO$_2$ static cell with high-speed jet distortions

Section 3.2 numerically demonstrated the superior performance of scanned-WMS-θ_{1f} over WMS-$nf/1f$ with respect to best-fit integrated absorbance accuracy under additive and multiplicative signal distortions below certain values
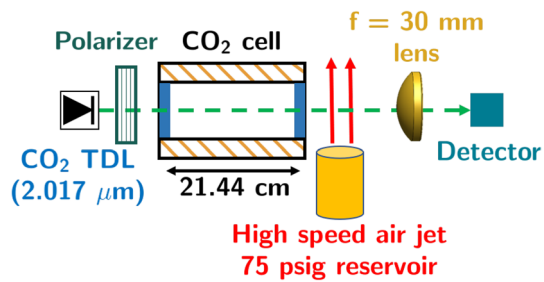
Fig. 16 Illustration of the experimental setup for the CO_2 detection experiments. The static CO_2 gas cell provided a constant gas absorption environment while the high-speed air jet and polarizer perturbed the transmitted intensity to simulate stochastic additive and multiplicative signal distortions

of p. To validate these findings, a series of CO_2 detection experiments were performed using a static optical gas cell and high-speed jet-induced optical perturbations. Figure 16 shows the experimental setup used for these experiments with major elements labeled. A fiber-coupled DFB-TDL (Nanoplus) operating near 2.017 μm was used to target the $P(24)$ absorption transition of the CO_2 $v = (2, 0, 1) \leftarrow (0, 0, 0)$ combination absorption band with vacuum linecenter near 4957.08 cm^{-1}. Light from the laser was collimated (Thorlabs F028APC-2000) and transmitted through a 21.44-cm-long optical gas cell capped with wedged sapphire windows. The laser was controlled and modulated with an Arroyo Instruments 6305 controller and a National Instruments USB-6353 waveform generator, respectively. Photodetector voltage and waveform generator timing pulses were collected and digitized by a Pico Technologies PicoScope 4824 at a rate of 10 MS s^{-1}. Mixtures of CO_2 diluted in N_2 were prepared manometrically within the gas cell using high-purity CO_2 and N_2 gas bottles (Praxair) and a barometer (Setra).

A high-speed air jet fed with a 75 psig reservoir was mounted immediately downstream of the gas cell to generate turbulence-induced density gradients that perturb the path of the transmitted light. Beam-steering experiments with the laser beam placed near the jet exit suggested a preferred Kelvin–Helmholtz instability mode near 52 kHz. This preferred mode quickly transitioned into fully developed turbulence beyond two jet diameters away from the exit plane (see [31]), thereby approximating stochastic broadband multiplicative distortions in the transmitted intensity. The transmitted laser intensity was collected by an anti-reflection-coated $f = 30$ mm CaF_2 lens and measured by an InGaAs photodetector (Thorlabs PDA10D). Because the distortion amplitude increases as the detector was moved away from the focus of the collection lens, the detector chip was not placed at the focus to control the amplitude of the air-jet distortions. Finally, a rotatable linear polarizer (Thorlabs LPMIR050) was placed between the laser and the static cell to variably
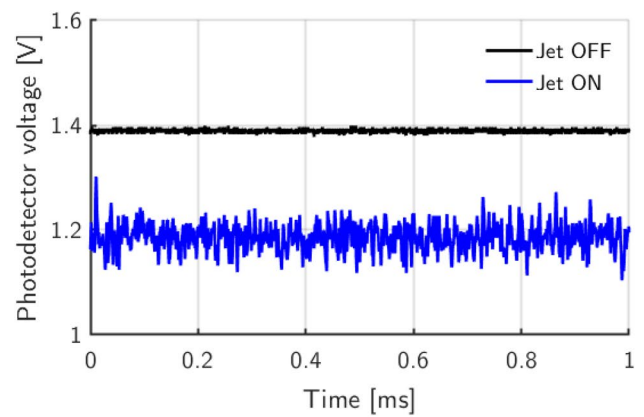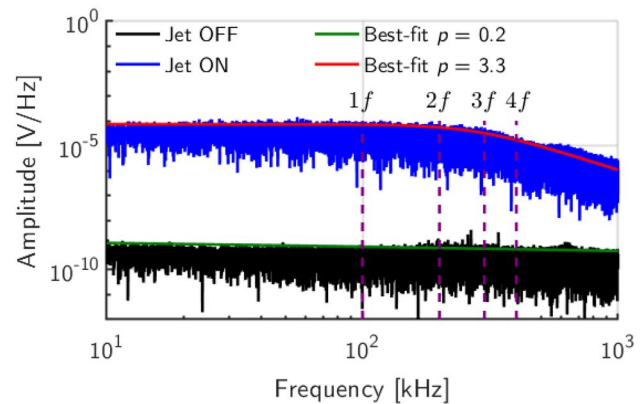
Fig. 17 Measured **a** time series and **b** frequency spectra of the transmitted intensity of a constant-intensity laser source with (black) and without (blue) distortions generated within the turbulent wake of a high-speed air jet. Power-law best-fits to the frequency spectra are shown in green and red

attenuate the incident laser intensity. This has the effect of boosting both the detection and electronics noise relative to the amplitude of the laser signal, thereby simulating an environment with stochastic additive signal distortions.

Figure 17 shows a sample photodetector (a) time series and (b) frequency spectrum (in log–log space) when the laser is operated at a constant intensity without (black) and with (blue) the air jet distortions. Both the time series and frequency spectra were vertically shifted in the figure for clarity. Without the jet distortions, the detection and digitization electronics noise exhibits a $p = 0.22$ decay exponent based on power-law fitting (shown in green in Fig. 17b) of the spectrum. Similarly, the best-fit to the jet distortions (shown in red in Fig. 17b) shows stochastic frequency content ranging from $f = 0$–1000 kHz with $f_{1/2} = 278$ kHz and $p = 3.3$. Note that it is possible to subject the various detection harmonics to different effective values of p by judiciously selecting appropriate modulation frequencies. For example, by choosing $f_m = 50$ kHz, the detection harmonics

up to $n = 4$ will experience essentially white noise ($p = 0$) distortions from the jet. Additionally, Fig. 17a essentially provides experimentally measured additive ($\kappa(t)$ in Eq. 15) and multiplicative ($\rho(t)$ in Eq. 16) distortion time series. With this information, identical $\kappa(t)$ and $\rho(t)$ signals can be used to distort multiple ideal $I_t(t)$ signals. This way, it is possible to compare the results of data collected from distinct μ–σ pairs across multiple hours without having to adjust for the temporal variability of the jet or electronics distortion spectra.

Figure 18 shows ϵ_A color-mapped onto a range of μ–σ pairs for (a) WMS-θ_{1f}, (b) -$2f/1f$, (c) -$3f/1f$, and (d) -$4f/1f$. These results were generated for $f_m = 100$ kHz, $f_s = 1$ kHz, and a static cell containing 9.59% CO_2 by mole in N_2 balance at a constant room temperature of 297 K and pressure of 1 atm. The IM–FM phase delay for this modulation frequency was measured to be 1.36π, well within the asymptotic region of Fig. 13. Brick-wall filters with cutoff frequency at $10f_s$ were used for the low-pass operation for computing the WMS harmonics. Concurrent

scanned-wavelength direct absorption spectroscopy (SDAS) measurements of the absorption spectrum indicated an $A_{known} = 0.05$ cm^{-1} and $\Delta\nu_C = 0.144$ cm^{-1}. The ideal transmitted intensity $I_t(t)$ for each μ–σ pair as measured by the photodetector was perturbed by rescaled versions of the $\rho(t)$ and $\kappa(t)$ distortion time series measured in Fig. 17. The rescaling factor was chosen such that the spectral power of $\rho(t)$ and $\kappa(t)$ at zero frequency were equal to 5% of the average transmitted intensity, which has the effect of setting $\xi_\kappa = 0.05\overline{I_0}$ and $\xi_\rho = 0.05$. At $f_m = 100$ kHz, the effective frequency roll-off exponent of the resulting distortion signal was equal to 0.92 based on power-law fitting of the frequency spectrum within the 100–400 kHz range.

Note that Fig. 18 is heavily undersampled in the μ–σ domain relative to Fig. 10 due to the extensive amount of time needed to collect data for the 252 distinct (μ, σ) pairs shown here. Nevertheless, it is possible to observe several trends from these results.
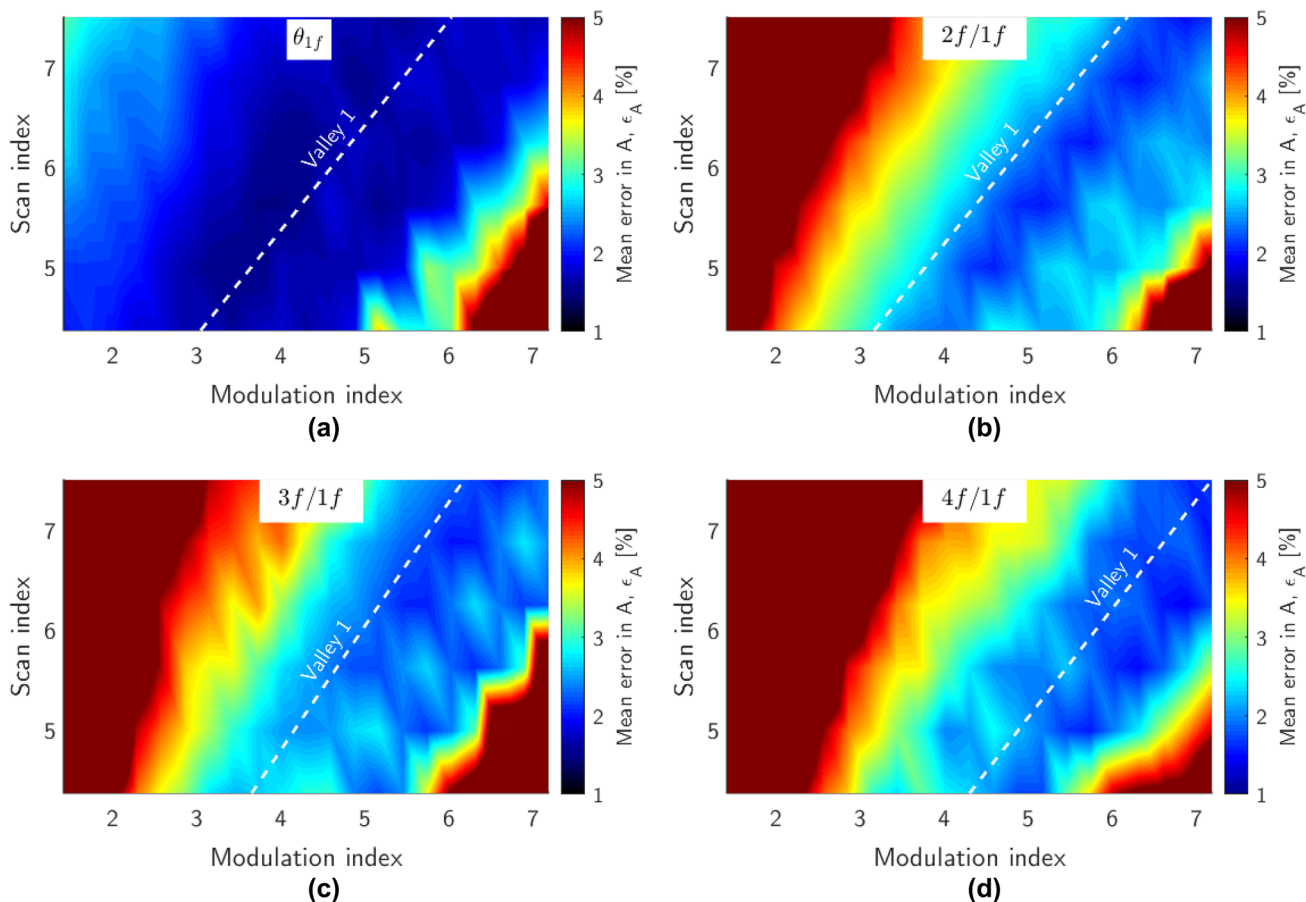

Fig. 18 Sample-averaged error the best-fit integrated absorbance, ϵ_A, color-mapped onto a matrix of scan and modulation index pairs for experimentally measured **a** WMS-θ_{1f}, **b** $2f/1f$, **c** $3f/1f$ and **d** $4f/1f$ signals distorted by experimentally measured jet-induced beam-steering and electronics noise with an effective $p = 0.92$. Identical optimal trough equations from Fig. 10 were superposed in dotted white lines to illustrate the close agreement between the simulated and measured optimal valleys

1. The data exhibit valleys of optimal μ–σ pairs identical to what was observed in Fig. 10. The trough equations in Fig. 10 were superimposed onto Fig. 18 with white dotted lines to illustrate the near perfect alignment between the simulated and measured optimal valleys.

2. Along the valleys, ϵ_A for WMS-θ_{1f} is, in general, lower than ϵ_A for the various WMS-nf/$1f$ methods, with WMS-$2f$ / $1f$, $3f$ / $1f$, and $4f$ / $1f$ performing on average 22%, 31%, and 20% worse than WMS-θ_{1f}, respectively. This is consistent with the results in 3.2.3, where it is expected that WMS-θ_{1f} performs better than -nf/$1f$ for $p = 0.92$.

Concurrent SDAS measurements using identical measurement rates, $\rho(t)$ and $\kappa(t)$ distortion time series, and the optimal SDAS modulation index, μ^*, of 5.6 were found exhibit an ϵ_A of 2.91%, a value greater than the minimum ϵ_A for all of the WMS methods shown in Fig. 18. This is consistent with the findings in Sect. 3.4 and "Appendix", which predicted that the accuracy of SDAS-based sensors will be worse than WMS-based sensors for stochastic distortion environments characterized by values of p near 1.

4.2 Flat-flame burner H₂O speciation and thermometry demonstration

The experimental setup shown in Fig. 19 was used as a practical demonstration of the WMS-θ_{1f} technique. Two fiber-coupled DFB-TDLs (NEL Photonics) were used to probe H_2O transitions near 7185.59 and 6806.06 cm^{-1} (1391.7 and 1469.3 nm, respectively) to measure the temperature and mole fraction of H_2O within the exhaust stream of a premixed CH_4/air flat-flame burner. Light from the two lasers was fiber-combined, collimated, and transmitted through the 25.4-cm-long burner apparatus and collected with an InGaAs photodetector. To maximize flame-induced distortions on the measured signals, a focusing lens was not installed in front of the photodetector. Transition linestrengths measured in Goldenstein et al. [33] were used to calculate temperature based on the best-fit integrated ab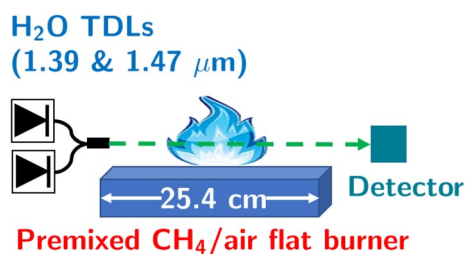sorbance of the two transitions. The laser targeting the transition near 7185.59 cm^{-1} was modulated and scanned at $(f_m, f_s) = (200, 1)$ kHz with optical tuning depths of $(a_{m,1}, a_{s,1}) = (0.138, 0.209)$ cm^{-1}, roughly corresponding to $(\mu, \sigma) = (3, 4.3)$ for typical combustion product stream composition and temperatures. Similarly, the laser targeting the transition near 6806.06 cm^{-1} was modulated and scanned at $(f_m, f_s) = (250, 1)$ kHz with optical tuning depths of $(a_{m,1}, a_{s,1}) = (0.097, 0.140)$ cm^{-1}, which also roughly corresponded to $(\mu, \sigma) = (3, 4.3)$ at typical burner conditions. This μ–σ pair is located within the trough labeled as "Valley 1" in Fig. 10a. IM–FM phase offsets were measured to be 1.21π and 1.28π for the 7185.59 and 6806.06 cm^{-1} lasers, respectively. The scanning frequency of 1 kHz provided a measurement rate of 2 kHz (one measurement per up- or down-scan). Brick-wall filters with cutoff frequency at $10f_s$ were used to compute the WMS harmonics.

Figure 20a shows examples of the measured and best-fit WMS-θ_{1f} for the absorption transition near 7185.59 cm^{-1} probing a CH_4/air mixture with equivalence ratio, Φ, of one. Data were collected over a period of 1 s and processed using WMS-θ_{1f}, $2f$/$1f$, and $3f$/$1f$ spectral fitting, yielding 2000 measurement samples across the collection period. Figure 20b shows the measured temperature and mole fraction time series processed using WMS-θ_{1f}. Long timescale fluctuations in both measurements reflect physical unsteadiness in the flame whereas short timescale fluctuations represent non-physical measurement uncertainties resulting from environmental signal distortions. Figure 20c, d shows the Allan deviation of the measured H_2O mole fraction and temperature, respectively, for WMS-θ_{1f}, -$2f$/$1f$, and -$3f$/$1f$. For both measurements, the WMS-θ_{1f} technique shows lower Allan deviations than either WMS-$2f$/$1f$ or WMS-$3f$/$1f$ regardless of the integration time, a result consistent with experimental observations in Yang et al. [14] and which demonstrates the benefits of using WMS-θ_{1f} for practical sensing.

5 Conclusion

A theoretical description of the scanned-wavelength WMS-θ_{1f} gas sensing technique and its associated spectral fitting algorithm was presented. The expected performance of the θ_{1f} strategy was directly compared against the popular WMS-nf/$1f$ and SDAS measurement techniques using simulations-based analyses of common signal distortions experienced in harsh measurement environments. The simulations were then experimentally validated in a static-gas-cell experiment subjected to broadband additive and multiplicative signal distortions. The WMS-θ_{1f} strategy exhibits several important characteristics.
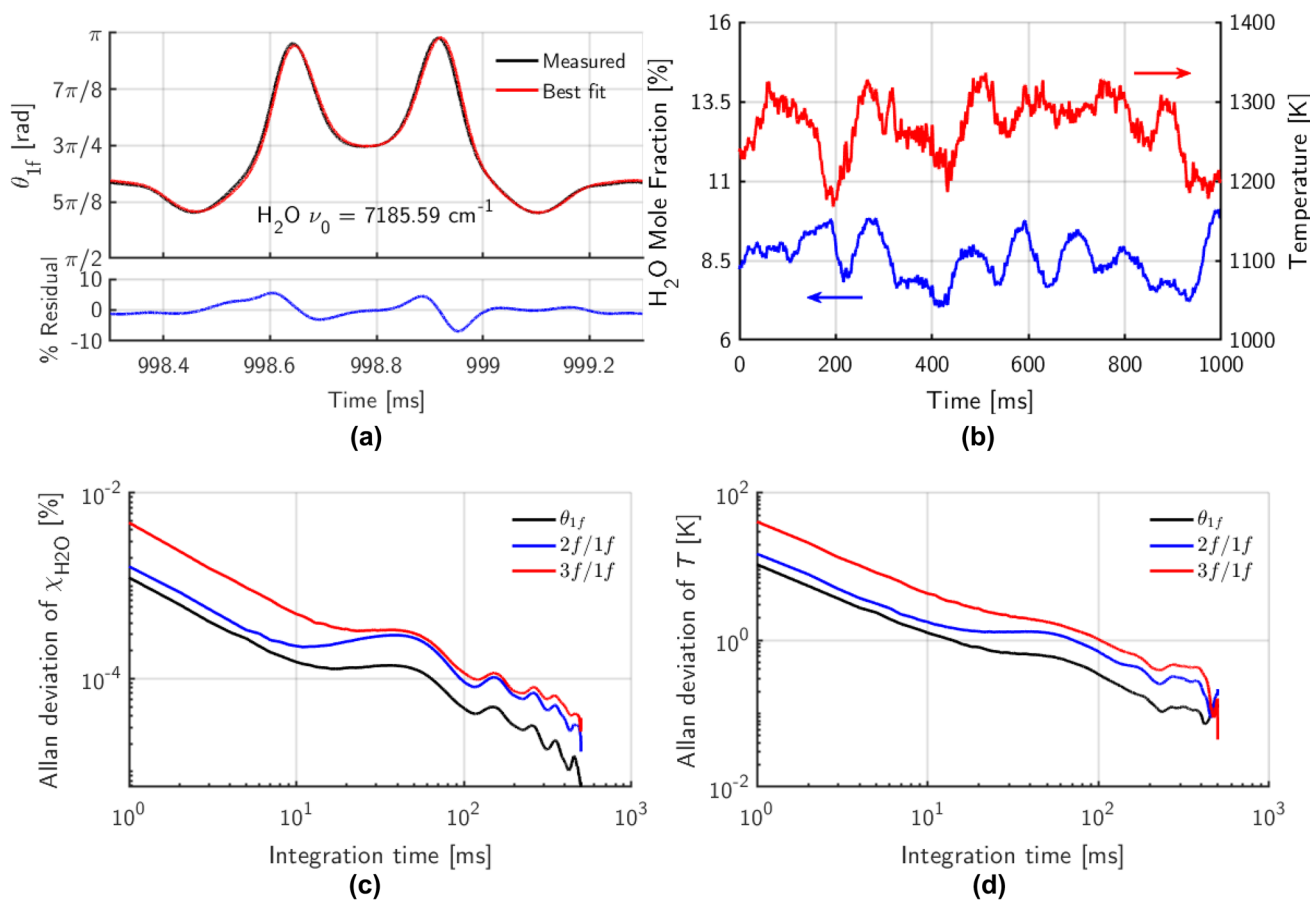
H₂O TDLs
(1.39 & 1.47 μm)

25.4 cm

Detector

Premixed CH₄/air flat burner

Fig. 19 Illustration of the experimental setup for H_2O concentration and temperature detection within the exhaust of a flat CH_4/air burner

(a)

(b)

(c)

(d)

Fig. 20 **a** Sample spectral fit of the WMS-θ_{1f} signal for the H_2O absorption transition near 7185.59 cm^{-1}. **b** Measured 1-s temperature (red) and H_2O mole fraction (blue) time-histories using the WMS-θ_{1f} technique within the exhaust of a CH_4/air flat-flame burner operating at equivalence ratio of 1. Allan deviations of **c** H_2O mole fraction and **d** temperature of the various WMS techniques for the same data set shown in **b**

1. Like WMS-nf/$1f$, WMS-θ_{1f} signals are immune to non-absorbing transmission losses and interfering emission with frequencies less than $f_m/2$. Additionally, the sensitivity of θ_{1f} signal to absorption lineshape enables the simultaneous fitting of lineshape parameters without prior knowledge or models of their behavior.

2. Both the optical scan and modulation depth parameters are important drivers of measurement accuracy for WMS-based sensors subjected to broadband environmental distortion. In contrast with the standard optimization strategy of selecting a modulation depth that maximizes the peak WMS response, the proposed method used in this work simultaneously optimizes the two parameters for a given measurement environment.

3. There exist certain ranges of frequency roll-off exponent, p, in the distortion spectrum at which WMS-θ_{1f} is expected to perform better than the various WMS-nf/$1f$ strategies. For the simulations, lasers, and detection systems used in this work, θ_{1f} was shown to be the preferred measurement technique for distortion signals that roll off slower than $1/f^{1.25}$ in the region of frequencies containing the detection harmonics.

4. For stochastic distortion environments with values of p near zero, SDAS is expected to perform better than the various WMS-nf/$1f$ methods regardless of the selected laser tuning parameters. However, WMS-θ_{1f} performance is generally on par with SDAS for $p = 0$, demonstrating that WMS-θ_{1f} is a suitable substitute for SDAS in applications with distortions exhibiting weak frequency dependence in the spectral amplitude.

5. Like WMS-nf/$1f$, the modulation depth of WMS-θ_{1f} signals can be chosen such that the results are insensitive to wavelength-dependent optical distortions. WMS-θ_{1f} measurements were also found to be insensitive to étalon interference patterns with low free spectral range, opposite the behavior of SDAS measurements.

It is clear from these results that WMS-θ_{1f} offers several potential benefits over traditional WMS-nf/$1f$ and SDAS strategies for high-precision measurements of gas parameters

in harsh measurement environments. Future research seeks to deploy θ_{1f}-based sensors for practical applications as well as to extend the analysis techniques developed in this work for selecting optimal laser-tuning parameters that maximize the accuracy of the best-fit $\Delta\nu_C$ and ν_0 parameters for pressure and velocimetry applications, respectively.

Additionally, the measurement technique-agnostic analysis procedures introduced in this work provide, to the authors' knowledge, the first set of tools for sensor designers to directly compare the relative performance of different TDLAS techniques for a given measurement application. These tools are expected to aid sensor designers in determining the true optimal sensing strategy and laser tuning parameters for any target environment.

6 Appendix: SDAS signal distortion analysis

The intensity and optical frequency tuning waveforms of a typical SDAS sensor can be described with sawtooth functions as follows:

$$I_0(t) = 2\overline{I_0}\big(2f_st - \lfloor 2f_st \rfloor\big) \tag{22}$$

$$\nu(t) = -2a_{m,1}\big(2f_st - \lfloor 2f_st \rfloor\big) + a_{m,1}. \tag{23}$$

Here, $\lfloor \ \rfloor$ is the floor function used to compute the sawtooth function. The definitions of $\overline{I_0}$, $a_{m,1}$, and f_s are consistent with the conventions used in Eqs. 6 and 7 for scanned-WMS signals. These definitions are also consistent with the conventions used to define modulation index, μ (Eq. 8), and non-dimensionalized wavelength-dependent distortion parameter, η (Sect. 3.3). Note that the frequency of the sawtooth was set at $2f_s$ to yield a SDAS measurement rate equal to the $2f_s$ measurement rate of scanned-WMS sensors.

6.1 Additive and multiplicative distortions

To directly compare the WMS-specific results in Sect. 3.2 against SDAS, $I_0(t)$ from Eq. 22 was attenuated and distorted by the same absorption spectrum and $\kappa(t)$ and $\rho(t)$ distortion time series as defined by the parameters listed in Table 1 to yield $\widetilde{I_t(t)}$. The distorted transmitted intensity was then used to compute the distorted absorption spectrum, $\widetilde{\alpha_\nu}$. Each measurement period was then fitted with Voigt profiles [2] to yield the best-fit spectroscopic parameters. An example of this distortion and its effect on the best-fit integrated absorbance is shown in Fig. 21, with the distortions introducing a 0.262% error in the best-fit integrated absorbance relative to the known value.

Using the analysis methods described in Sect. 3, it is possible to compute the sample-averaged error in the best-fit
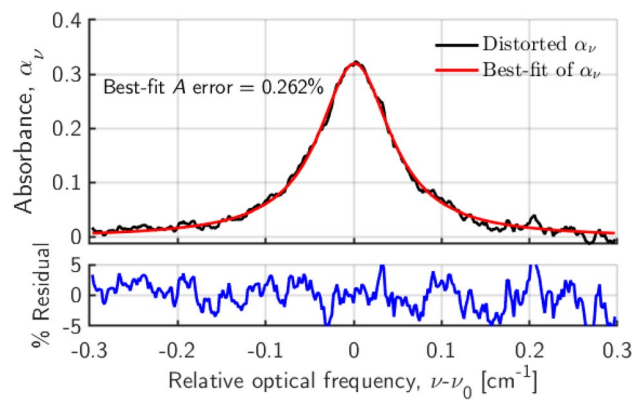

Fig. 21 Example effect of stochastic $1/f$ additive and multiplicative signal distortions on the measured spectral absorbance (black, top panel) and the resulting best-fit absorbance (red, top panel) and residual (bottom panel). Parameters used to simulate these results are listed in Table 1. The distortions introduced a 0.262% error in the best-fit integrated absorbance relative to the known value
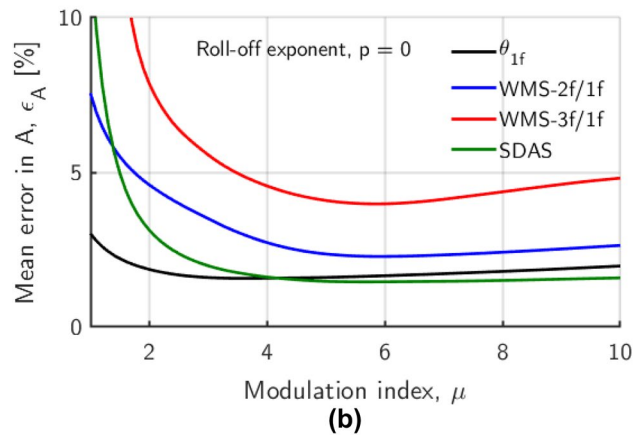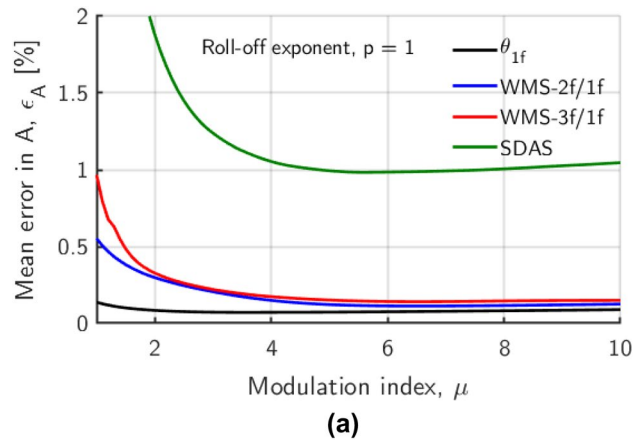

Fig. 22 Sample-averaged error in the best-fit integrated absorbance for SDAS (green), WMS-θ_{1f} (black), -2f/1f (blue), and -3f/1f (red) as a function of modulation index, μ, when perturbed by stochastic additive and multiplicative noise with roll-off exponent, p, equal to **a** 1, and **b** 0. μ-σ pairs for the WMS methods follow the linear relationship labeled as "Valley 2" in Fig. 10. Parameters used to simulate these results are listed in Table 1
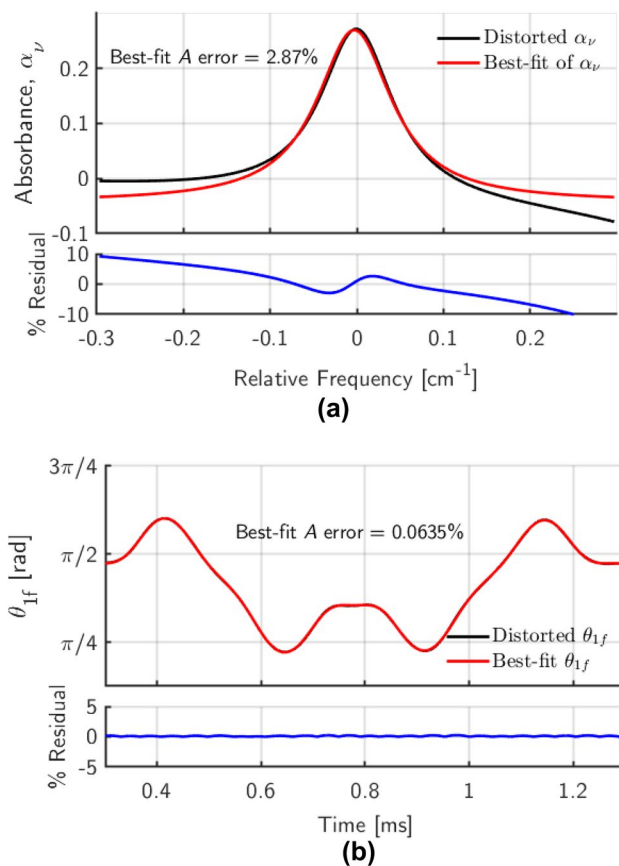
Fig. 23 Example effect of pure-tone additive and multiplicative distortions on measured **a** SDAS spectra and **b** WMS-θ_{1f} signals. In both cases, the ideal transmitted intensity was perturbed by pure-tone sinusoidal distortion time series with frequency $f_s/10$ and $f_m/10$ for SDAS and WMS-θ_{1f}, respectively. Note that the distortions negligibly affect the WMS-θ_{1f} spectrum due to the lock-in filtering and intensity normalization operations
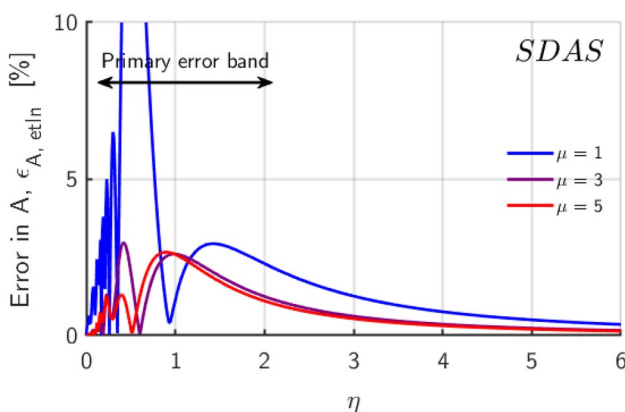

Fig. 24 Étalon-induced errors in the best-fit integrated absorbance of SDAS measurements as a function of η. The distortion amplitude was set at 1% of the peak absorbance. Each curve represents a different value of modulation index

integrated absorbance, ϵ_A, for SDAS measurements as a function of μ, which is shown in green in Fig. 22a. Superposed on Fig. 22a are the ϵ_A for WMS-θ_{1f} (black), -2f/1f (blue), and -3f/1f (red) evaluated along the valleys of optimal μ–σ shown in Fig. 10 ("Valley 2" for each WMS technique was used since they contain the global optima). Several trends can be observed from these results.

1. ϵ_A for SDAS is consistently higher than the various WMS measurement techniques assuming the roll-off exponent, p, is equal to 1. This trend agrees with intuition because the frequency content of the distortion time series are primarily concentrated at low frequencies with $f < f_{1/2}$, which in these simulations correspond to $f < 10f_s$. Since SDAS does not filter or correct for low-frequency noise signatures, it is expected that the performance of SDAS will be more heavily impacted by the distortions than WMS.

2. There exists an optimal $\mu^* = 5.6$ that minimizes ϵ_A for SDAS sensors. To the authors' knowledge, this represents the first reported observation of optimal tuning parameters for SDAS sensors in the presence of environmental distortions. However, the ϵ_A–μ curve flattens and becomes largely insensitive to μ at values of μ larger than 5.6, indicating that it is not severely detrimental to SDAS sensor performance if the laser is over-modulated beyond $\mu = 5.6$. This characteristic is critical for applications where multiple absorption transitions are simultaneously measured within each laser scan.

We also evaluated the case where the additive and multiplicative distortion signals exhibit uniform power in the frequency domain (i.e. $p = 0$ or white noise). This is an important test case for practical applications because the primary sources of stochastic signal distortions in quiescent environments (e.g. static cells or environmental monitoring devices in general) are noise in the light detection and electronic digitization hardware, which often exhibit roll-off exponents close to zero (as evidenced in Fig. 17b). The results of this exercise are shown in Fig. 22b. As can be seen, when subjected to $p = 0$ distortions, SDAS performs better than the various WMS-$nf/1f$ techniques while rivaling the performance of WMS-θ_{1f} sensors. These observations suggest that, for certain environments with stochastic distortions exhibiting sufficiently low p, implementing WMS instead of SDAS may actually be detrimental to sensor performance.

Although the preceding results demonstrate that SDAS sensors perform comparably to WMS-based sensors for certain broadband, stochastic distortion environments, it is important to note that SDAS does not enjoy the benefits of intensity normalization and optical emission rejection that is inherent in the WMS-θ_{1f} and -$nf/1f$ techniques. When SDAS signals are perturbed by strong pure-tone additive and

multiplicative distortions (e.g. from natural vibrations in the measurement environment), it becomes difficult to infer an appropriate $I_0(t)$ from the measurement, resulting in significant errors. WMS-θ_{1f} and -nf/1f do not suffer from these difficulties because all additive and multiplicative distortions with frequency below $f_m/2$ are removed by the lock-in filter and intensity normalization operations. These distinctions are illustrated in Fig. 23, where pure-tone sinusoidal $\rho(t) = 1 + 0.1 \sin\left(\frac{2\pi f_s}{10}t\right)$ and $\kappa(t) = 0.1\overline{I_0}\sin\left(\frac{2\pi f_s}{10}t\right)$ distortion time series were used to perturb the SDAS absorption profile in Fig. 23a, resulting in a 2.87% error in the best-fit integrated absorbance. These results are compared against Fig. 23b, where pure-tone sinusoidal $\rho(t) = 1 + 0.1 \sin\left(\frac{2\pi f_m}{10}t\right)$ and $\kappa(t) = 0.1\overline{I_0}\sin\left(\frac{2\pi f_m}{10}t\right)$ distortion time series were used to perturb the WMS-θ_{1f} signal. As can be seen, the resulting WMS-θ_{1f} signal was negligibly affected by the pure-tone distortions, resulting in an error in the best-fit integrated absorbance of only 0.0635%.

It is worth noting that there are well-established post-processing techniques such as polynomial baseline fitting that can correct for signal distortions and somewhat improve the accuracy of SDAS measurements. For the example shown in Fig. 23a, a second-order polynomial fitting of the non-absorbing wings of the absorption transition yielded a best-fit integrated absorbance error of 0.59%, a significant improvement relative to the uncorrected signal. However, these techniques are generally artificial methods that add additional free parameters to the post-processing work flow that may not be grounded in reality. Additionally, polynomial baseline fitting cannot account for intra-scan additive offsets in $I_t(t)$ (e.g. due to optical emission), which would result in incorrect measurements of the absorbance. As a result, correction schemes for SDAS measurements are, at best, unreliable in highly dynamic environments. This is in contrast with WMS-θ_{1f} and -nf/1f, both of which correct for additive and multiplicative distortions by directly decoupling these distortions from the spectroscopic measurement a priori rather than through artificial corrections in post-processing.

6.2 A.2 Wavelength-dependent distortions

The procedures described in Sect. 3.3 were used to compute the average expected error in the best-fit integrated absorbance, $\epsilon_{A,\text{etln}}$, for an SDAS measurement distorted by étalon-like interference fringes. Figure 24 shows how the $\epsilon_{A,\text{etln}}$ of SDAS varies as a function of η for various values of μ. Like in Fig. 15, ξ_{etln} was set to be 1% of the peak absorbance.

Several observations can be made from comparing Fig. 24 against Fig. 15.

1. Like the various WMS methods considered in Fig. 15, $\epsilon_{A,\text{etln}}$ vanishes when η approaches zero or infinity and decreases in general with increasing μ.

2. The primary error band for SDAS is narrower than the bands for WMS-θ_{1f} and 2f/1f and is confined to lower values of η, indicating that short-period étalons most adversely impact the accuracy of SDAS sensors. This is the opposite of the behavior observed for WMS-θ_{1f} (Fig. 15a). In certain environments were cavity lengths are long (e.g. cavity-enhanced techniques) and, therefore, étalon free-spectral ranges are short, it may be advisable to use WMS-θ_{1f} to reduce sensitivity to wavelength-dependent distortions.

3. $\epsilon_{A,\text{etln}}$ within the primary error band for SDAS are, in general, less than either WMS-θ_{1f} or WMS-2f/1f, indicating that, at suboptimal values of η, SDAS may be more forgiving than WMS-based methods for wavelength-dependent distortions.

References

1. R.K. Hanson, Applications of quantitative laser sensors to kinetics, propulsion and practical energy systems. Proc. Combust. Inst. **33**(1), 1–40 (2011). https://doi.org/10.1016/j.proci.2010.09.007
2. C.S. Goldenstein, R.M. Spearrin, J.B. Jeffries, R.K. Hanson, Infrared laser-absorption sensing for combustion flows. Prog. Energy Combust. Sci. **60**, 132–176 (2016). https://doi.org/10.1016/j.pecs.2016.12.002
3. M. Lackner, Tunable diode laser absorption spectroscopy for gas sensing in the process industries—a review. Rev. Chem. Eng. (2007). https://doi.org/10.1515/REVCE.2007.23.2.65
4. J. Röpcke, G. Lombardi, A. Rousseau, P.B. Davies, Application of mid-infrared tuneable diode laser absorption spectroscopy to plasma diagnostics: a review. Plasma Sour. Sci. Technol. **15**(4), S148 (2006)
5. Z. Wang, P. Fu, X. Chao, Laser absorption sensing systems: challenges, modeling, and design optimization. Appl. Sci. (2019). https://doi.org/10.3390/app9132723
6. G. C. Mathews, C.S. Goldenstein, Wavelength-modulation spectroscopy for MHz thermometry and H2O sensing in combustion gases of energetic materials. AIAA Scitech Forum, pp. 1–8 (2019)
7. R.M. Spearrin, C.S. Goldenstein, I.A. Schultz, J.B. Jeffries, R.K. Hanson, Simultaneous sensing of temperature, CO, and CO2 in a scramjet combustor using quantum cascade laser absorption spectroscopy. Appl. Phys. B Lasers Opt. **117**(2), 689–698 (2014). https://doi.org/10.1007/s00340-014-5884-0
8. C.S. Goldenstein, R.M. Spearrin, J.B. Jeffries, R.K. Hanson, Infrared laser absorption sensors for multiple performance parameters in a detonation combustor. Proc. Combust. Inst. **35**(3), 3739–3747 (2014). https://doi.org/10.1016/j.proci.2014.05.027

9. D.D. Lee, F.A. Bendana, S.A. Schumaker, R.M. Spearrin, Wavelength modulation spectroscopy near 5 um for carbon monoxide sensing in a high-pressure kerosene-fueled liquid rocket combustor. Appl. Phys. B Lasers Opt. (2018). https://doi.org/10.1007/s00340-018-6945-6

10. C. A. Almodovar, D. Salazar, C. L. Strand, R. K. Hanson, R. G. Wright, C. M. Brophy, TDLAS measurements of the underexpanded exhaust plume from a solid propellant gas generator. AIAA Scitech Forum, pp. 1–10 (2019). https://arc.aiaa.org/doi/10.2514/6.2019-0028

11. W.Y. Peng, R. Sur, C.L. Strand, R.M. Spearrin, J.B. Jeffries, R.K. Hanson, High-sensitivity in situ QCLAS-based ammonia concentration sensor for high-temperature applications. Appl. Phys. B Lasers Opt. **122**, 188 (2016). https://doi.org/10.1007/s00340-016-6464-2

12. W.Y. Peng, S.J. Cassady, C.L. Strand, C.S. Goldenstein, R.M. Spearrin, C.M. Brophy, J.B. Jeffries, R.K. Hanson, Single-ended mid-infrared laser-absorption sensor for time-resolved measurements of water concentration and temperature within the annulus of a rotating detonation engine. Proc. Combust. Inst. **37**(2), 1435–1443 (2019). https://doi.org/10.1016/j.proci.2018.05.021

13. W.Y. Peng, Y. Wang, S.J. Cassady, C.L. Strand, R.K. Hanson, Single-ended sensor for thermometry and speciation in shock tubes using native surfaces. IEEE Sens. J. **19**(13), 4954–4961 (2019). https://doi.org/10.1109/JSEN.2019.2903989

14. C. Yang, L. Mei, H. Deng, Z. Xu, B. Chen, R. Kan, Wavelength modulation spectroscopy by employing the first harmonic phase angle method. Opt. Express **27**(9), 12137–12146 (2019). https://doi.org/10.1364/OE.27.012137

15. A. Upadhyay, M. Lengden, D. Wilson, G.S. Humphries, A.P. Crayford, D.G. Pugh, M.P. Johnson, G. Stewart, W. Johnstone, A new RAM normalized 1f-WMS technique for the measurement of gas parameters in harsh environments and a comparison with 2f/1f. IEEE Photon. J. **10**(6), 1–11 (2018)

16. C. S. Goldenstein, C. L. Strand, I. A. Schultz, K. Sun, J. B. Jeffries, R. K. Hanson, Fitting of calibration-free scanned-wavelength-modulation spectroscopy spectra for determination of gas properties and absorption lineshapes. Appl. Opt. **53**(3), 356–367 (2014).

17. G.B. Rieker, J.B. Jeffries, R.K. Hanson, Calibration-free wavelength-modulation spectroscopy for measurements of gas temperature and concentration in harsh environments. Appl. Opt. **48**(29), 5546–5560 (2009). https://doi.org/10.1364/AO.48.005546

18. J. Reid, D. Labrie, Second-harmonic detection with tunable diode lasers—comparison of experiment and theory. Appl. Phys. B Lasers Opt. **26**(3), 203–210 (1981). https://doi.org/10.1007/BF00692448

19. P. Kluczynski, O. Axner, Theoretical description based on Fourier analysis of wavelength-modulation spectrometry in terms of analytical and background signals. Appl. Opt. **38**(27), 5803–5815 (1999)

20. L.C. Philippe, R.K. Hanson, Laser diode wavelength-modulation spectroscopy for simultaneous measurement of temperature, pressure, and velocity in shock-heated oxygen flows. Appl. Opt. **32**(30), 6090–6103 (1993)

21. C. L. Strand, Scanned wavelength modulation absorption spectroscopy with application to hypersonic impulse flow facilities, Ph.D. dissertation, Stanford University (2014)

22. R.K. Hanson, R.M. Spearrin, C.S. Goldenstein, *Spectroscopy and optical diagnostics for Gases*, 1st edn. (Springer, New York, 2015)

23. K. Sun, X. Chao, R. Sur, C. S. Goldenstein, J. B. Jeffries, R. K. Hanson, Analysis of calibration-free wavelength-scanned wavelength modulation spectroscopy for practical gas sensing using tunable diode lasers. Meas. Sci. Technol. **24**(12), 1–12 (2013)

24. H. Li, G.B. Rieker, X. Liu, J.B. Jeffries, R.K. Hanson, Extension of wavelength-modulation spectroscopy to large modulation depth for diode laser absorption measurements in high-pressure gases. Appl. Opt. **45**(5), 1052–1061 (2006)

25. E. Polak, G. Ribiere, Note sur la convergence de méthodes de directions conjuguées. Revue française d'informatique et de recherche opérationnelle **3**(16), 35–43 (1969)

26. K. Levenberg, A method for the solution of certain non-linear problems in least squares. Quart. Appl. Math. **2**(2), 164–168 (1944)

27. D.W. Marquardt, An algorithm for least-squares estimation of nonlinear parameters. J. Soc. Ind. Appl. Math. **11**(2), 431–441 (1963)

28. W. Wei, W.Y. Peng, Y. Wang, R. Choudhary, S. Wang, J. Shao, R.K. Hanson, Demonstration of non-absorbing interference rejection using wavelength modulation spectroscopy in high-pressure shock tubes. Appl. Phys. B Lasers Opt. **125**(9), 1–10 (2019). https://doi.org/10.1007/s00340-018-7118-3

29. R. Sur, K. Sun, J.B. Jeffries, J.G. Socha, R.K. Hanson, Scanned-wavelength-modulation-spectroscopy sensor for CO, CO2, CH4 and H2O in a high-pressure engineering-scale transport-reactor coal gasifier. Fuel **150**, 102–111 (2015). https://doi.org/10.1016/j.fuel.2015.02.003

30. W.S. Kendal, B. Jørgensen, Tweedie convergence: a mathematical basis for Taylor's power law, 1/f noise, and multifractality. Phys. Rev. E Stat. Nonlinear Soft Matter Phys. **84**(6), 1–10 (2011)

31. H. Winarto, M. Davis, Fluctuations of density, pressure and temperature in a turbulent mixing region. Proc. R. Soc. Lond. Series A Math. Phys. Sci. **395**(1809), 203–228 (1984)

32. S. J. Cassady, W. Y. Peng, C. L. Strand, J. B. Jeffries, R. K. Hanson, D. F. Dausen, C. M. Brophy, A single-ended, mid-IR sensor for time-resolved temperature and species measurements in a hydrogen/ethylene-fueled rotating detonation engine. AIAA SciTech Forum, pp. 1–8 (2019)

33. C. S. Goldenstein, R. K. Hanson, Diode-laser measurements of linestrength and temperature-dependent lineshape parameters for H_2O transitions near 1.4μm using Voigt, Rautian, Galatry, and speed-dependent Voigt profiles. J. Quant. Spectrosc. Radiat. Transfer. **152**, 127–139 (2015)